AD-A062 724 CALIFORNIA UNIV BERKELEY ELECTRONICS RESEARCH LAB F/G 20/9
FIRST QUARTER PROGRESS REPORT ON PLASMA THEORY AND SIMULATION.(U)
APR 78 C K BIRDSALL N00014-77-C-0578

UNCLASSIFIED NL

/ OF /
AD
A062724

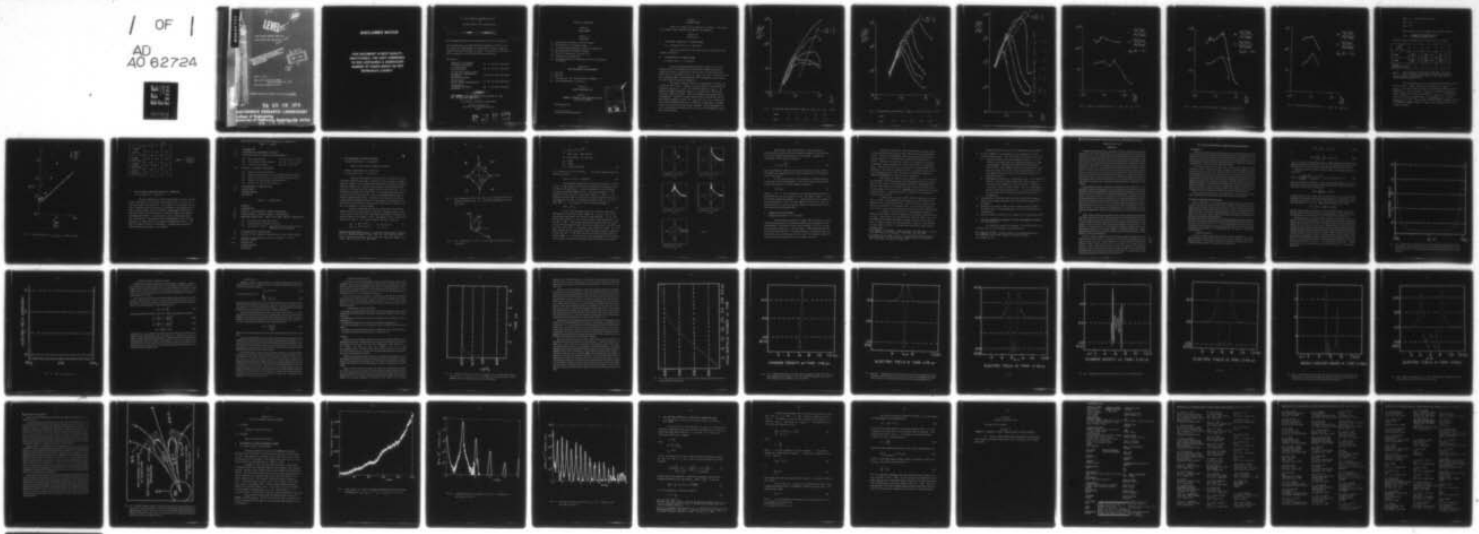

END
DATE
FILMED
3-79
DDC

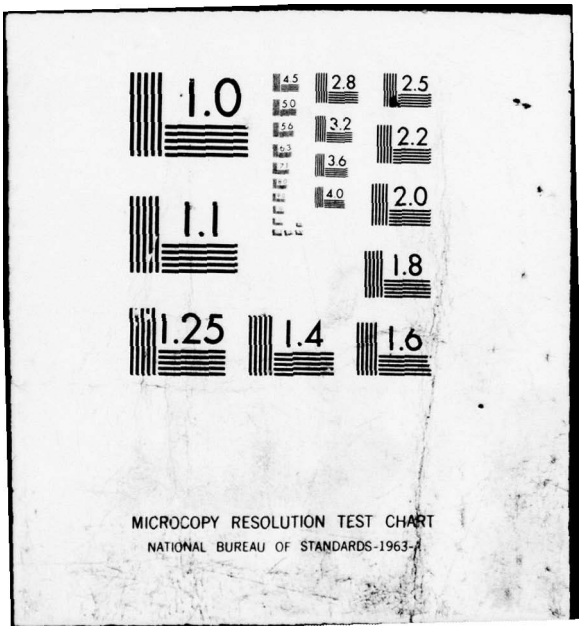
1.0
1.1
1.25
1.4
1.6
1.8
2.0
2.2
2.5
2.8
3.2
3.6
4.0
4.5
5.0
5.6
6.3
MICROCOPY RESOLUTION TEST CHART
NATIONAL BUREAU OF STANDARDS-1963-A

AD A062724

NR 012-
ONR 421

12
B.S.

LEVEL III

FIRST QUARTER PROGRESS REPORT ON PLASMA THEORY AND SIMULATION

A06 2 725

THIS DOCUMENT IS BEST QUALITY PRACTICABLE.
THE COPY FURNISHED TO DDC CONTAINED A
SIGNIFICANT NUMBER OF PAGES WHICH DO NOT
REPRODUCE LEGIBLY.

DDC
DEC 29 1978
F

April 1, 1978

ERDA Contract EY-76-S-03-0034
(Project Agreement No. 128)

ONR Contract N00014-77-C-0578

APPROVED FOR PUBLIC RELEASE; DISTRIBUTION UNLIMITED

78 09 28 078

ELECTRONICS RESEARCH LABORATORY
College of Engineering
University of California, Berkeley, CA 94720

78 12 26 123

DISCLAIMER NOTICE

THIS DOCUMENT IS BEST QUALITY PRACTICABLE. THE COPY FURNISHED TO DDC CONTAINED A SIGNIFICANT NUMBER OF PAGES WHICH DO NOT REPRODUCE LEGIBLY.

FIRST QUARTER PROGRESS REPORT
on
PLASMA THEORY and SIMULATION

Rept. for 1 January 1 - 31 March 31, 1978,

54p.

Work accomplished during the First Quarter of 1978 is reported here.

Our research group uses both theory and simulaton as tools in order to increase the understanding of instabilities, heating, diffusion, transport and other phenomena in plasma. We also work on the improvement of simulation, both theoretically and practically.

Our staff is:

Professor C. K. Birdsall (Principal Investigator)	191	M	Cory Hall (642-4015)
Dr. Yoshi Matsuda (Post Doctorate)	119	ME	Cory Hall (642-3477)
Yu Jiuan Chen, Douglas Harned, Jae Koo Lee, William Nevins, Ali Peiravi (Research Assistants)	119	MD	Cory Hall (642-1297)
William Fawley (Guest, from UC Astronomy Dept.)	119	MD	Cory Hall (642-1297)
Mike Hoagland (Technical Information Specialist)	199	M	Cory Hall (642-7919)

1 April 1978

ERDA Contract EY-76-S-03-0034 (Project Agreement No. 128)
ONR Contract N00014-77-C-0578

ELECTRONICS RESEARCH LABORATORY

College of Engineering
University of California, Berkeley
94720

127 550

78 12 26 025
78 09 28 078

TABLE of CONTENTS*

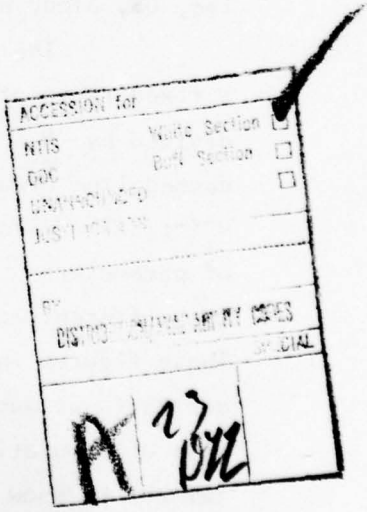

* Indicates ONR supported area.

Section I
PLASMA THEORY

There is no report for this Section this quarter. The remainder of Nevins' work, reported last quarter, was completed.

Section II
SIMULATION

A. QUASILINEAR SIMULATION OF A MIRROR MACHINE

Dr. Y. Matsuda with Dr. H. L. Berk (LLL)

While work continues in this area, there is no special report to make this quarter.

B. SELF-HEATING OF 1d THERMAL PLASMA

A. Peiravi (Prof. C. K. Birdsall)

We have already presented simulation results for the self-heating times of a one-dimensional electrostatic thermal plasma and a comparison of cost of simulation vs heating time. We now present complete results of self-heating times vs $\omega_{pe}\Delta t$ and $\lambda_D/\Delta x$ for nearest grid point weighting, NGP, linear weighting, CIC, and quadratic spline weighting, QS, along with gain considerations.

The heating time was found to be proportional to $N_C + N_D$ for a fixed ratio of $\lambda_D/\Delta x$. Figures 1,2, and 3 show the self-heating times divided by $N_C + N_D$ vs $\lambda_D/\Delta x$ for different values of $\omega_{pe}\Delta t$. The dashed line drawn through the figures is $v_t(\Delta t/\Delta x) \approx 3/2$ for NGP and $v_t(\Delta t/\Delta x) \simeq 1/2$ for CIC and QS. These lines indicate the optimal choices of parameters. Figures 4, 5, and 6 show ratios of self-heating times of the different weights vs $\lambda_D/\Delta x$ for $\omega_{pe}\Delta t = 0.1, 0.2, 0.3$, respectively. These figures indicate that CIC is as much as 70 times better than NGP, and QS is as much as 650 times better than NGP. Actual measurements of cost of simulation per particle per time step on the CDC-7600 MFE computer at LLL show that

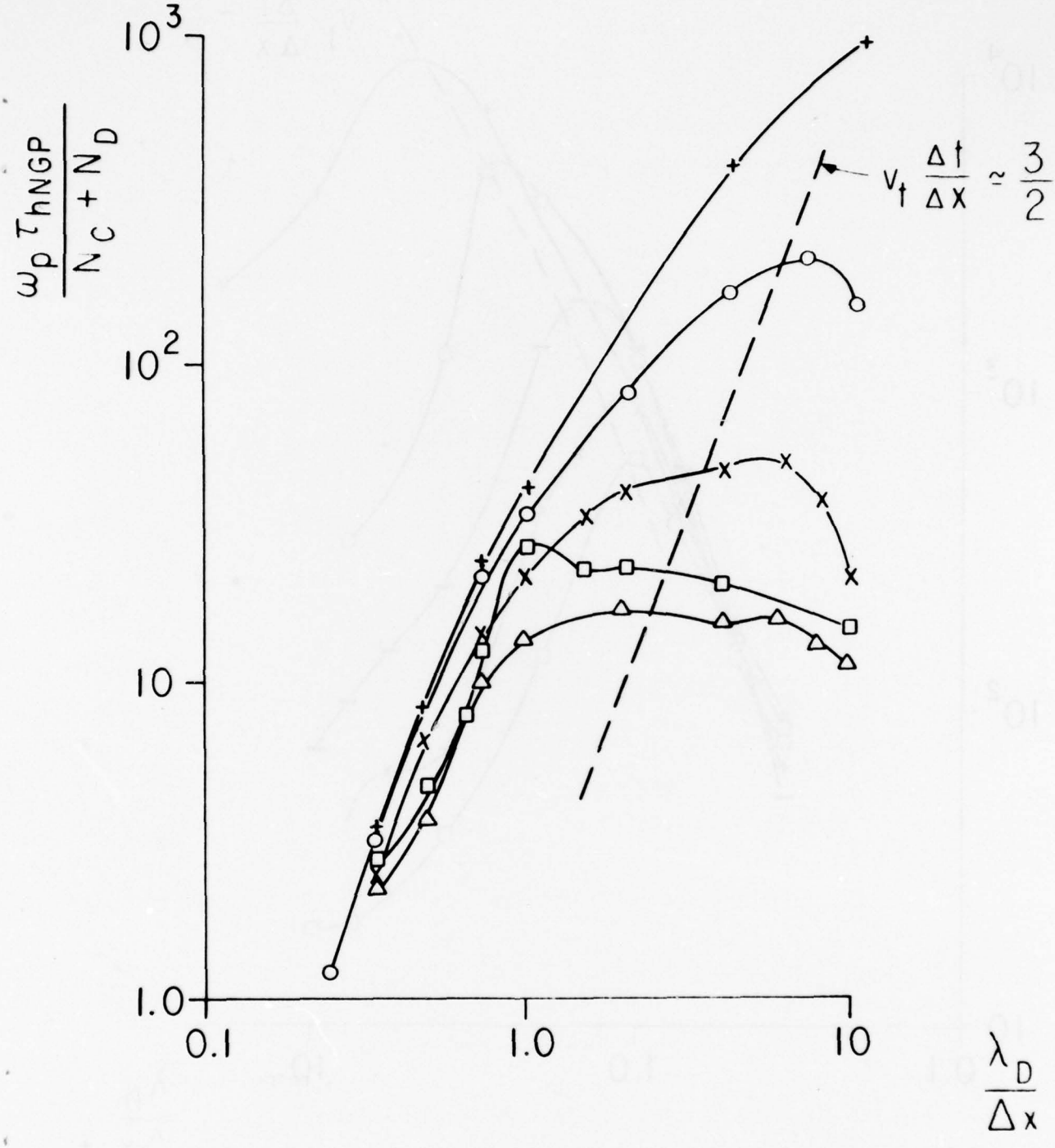

Fig. 1 Self-heating times divided by N_C+N_D vs $\lambda_D/\Delta x$ for $\omega_{pe}\Delta t$ for NGP.

symbol	+	o	×	□	Δ
$\omega_{pe}\Delta t$	0.1	0.2	0.4	0.5	0.6

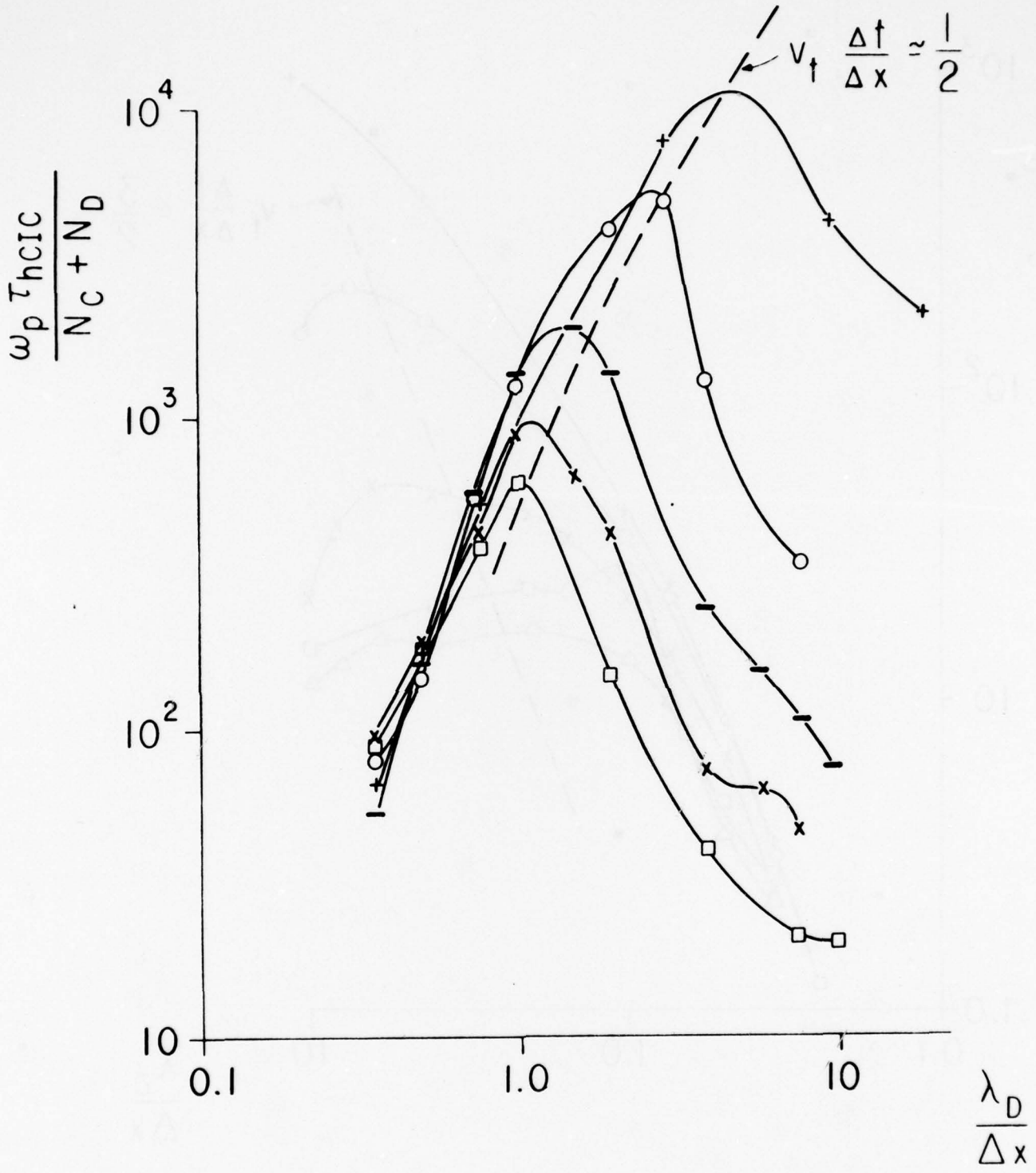

FIG. 2 Self-heating times divided by N_C+N_D vs $\lambda_D/\Delta x$ for $\omega_{pe}\Delta t$ for CIC.

symbol	+	o	-	x	□
$\omega_{pe}\Delta t$	0.1	0.2	0.3	0.4	0.5

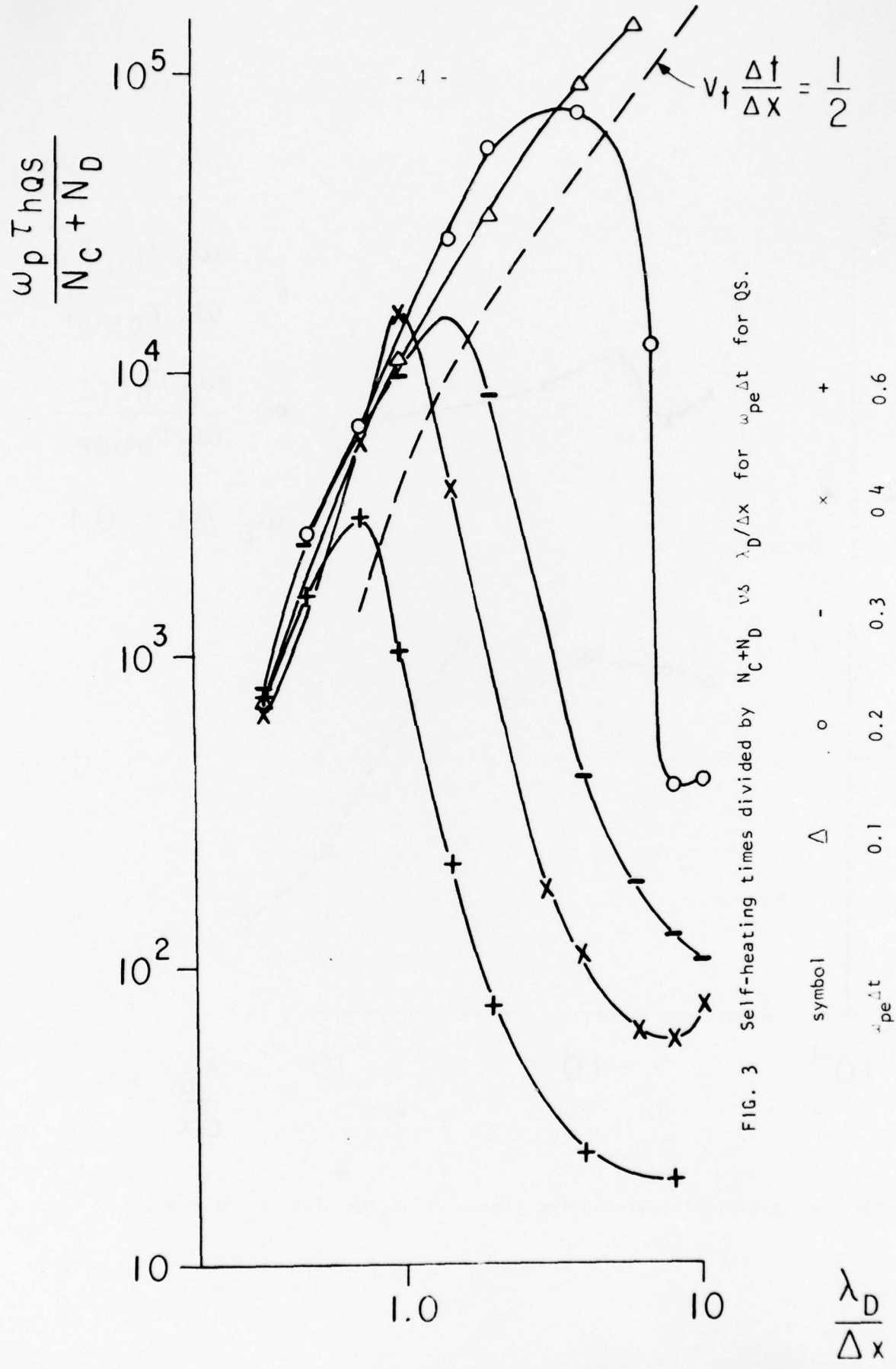

FIG. 3 Self-heating times divided by N_C+N_D vs $\lambda_D/\Delta x$ for $\omega_{pe}\Delta t$ for QS.

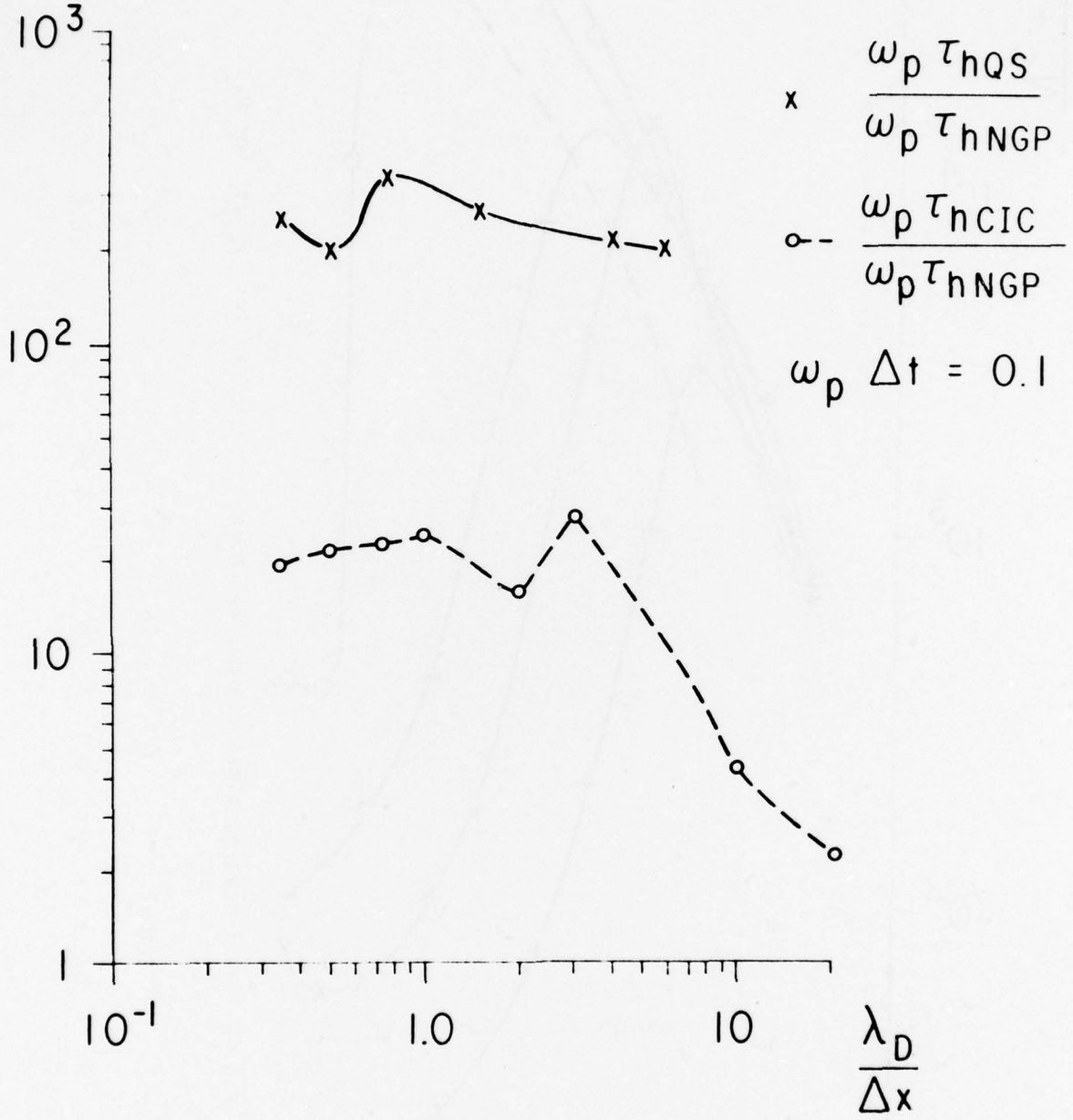

FIG. 4 Ratios of self-heating times vs $\lambda_D/\Delta x$ for $\omega_{pe}\Delta t = 0.1$.

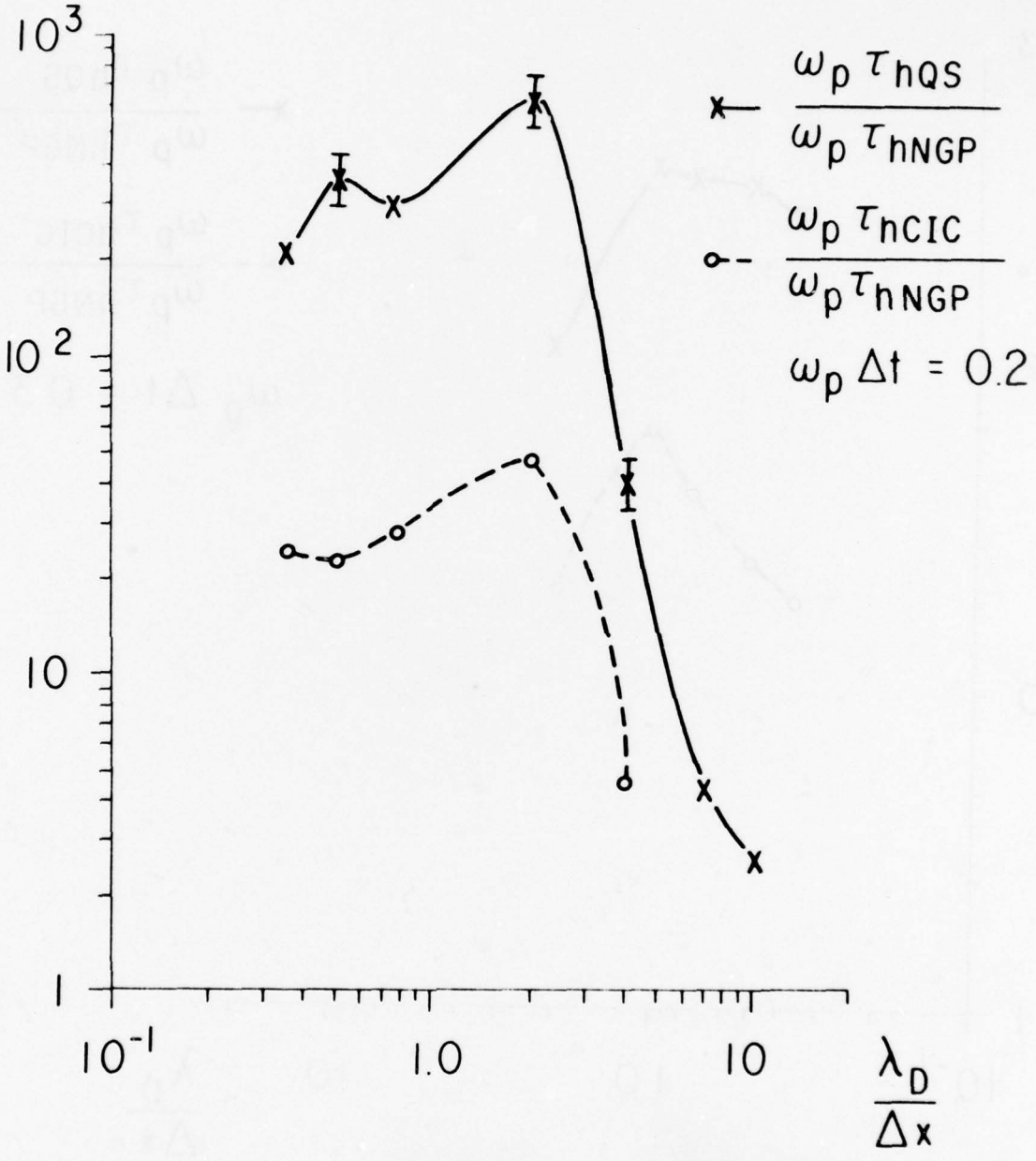

FIG. 5 Ratios of self-heating times vs $\lambda_D/\Delta x$ for $\omega_{pe}\Delta t = 0.2$.

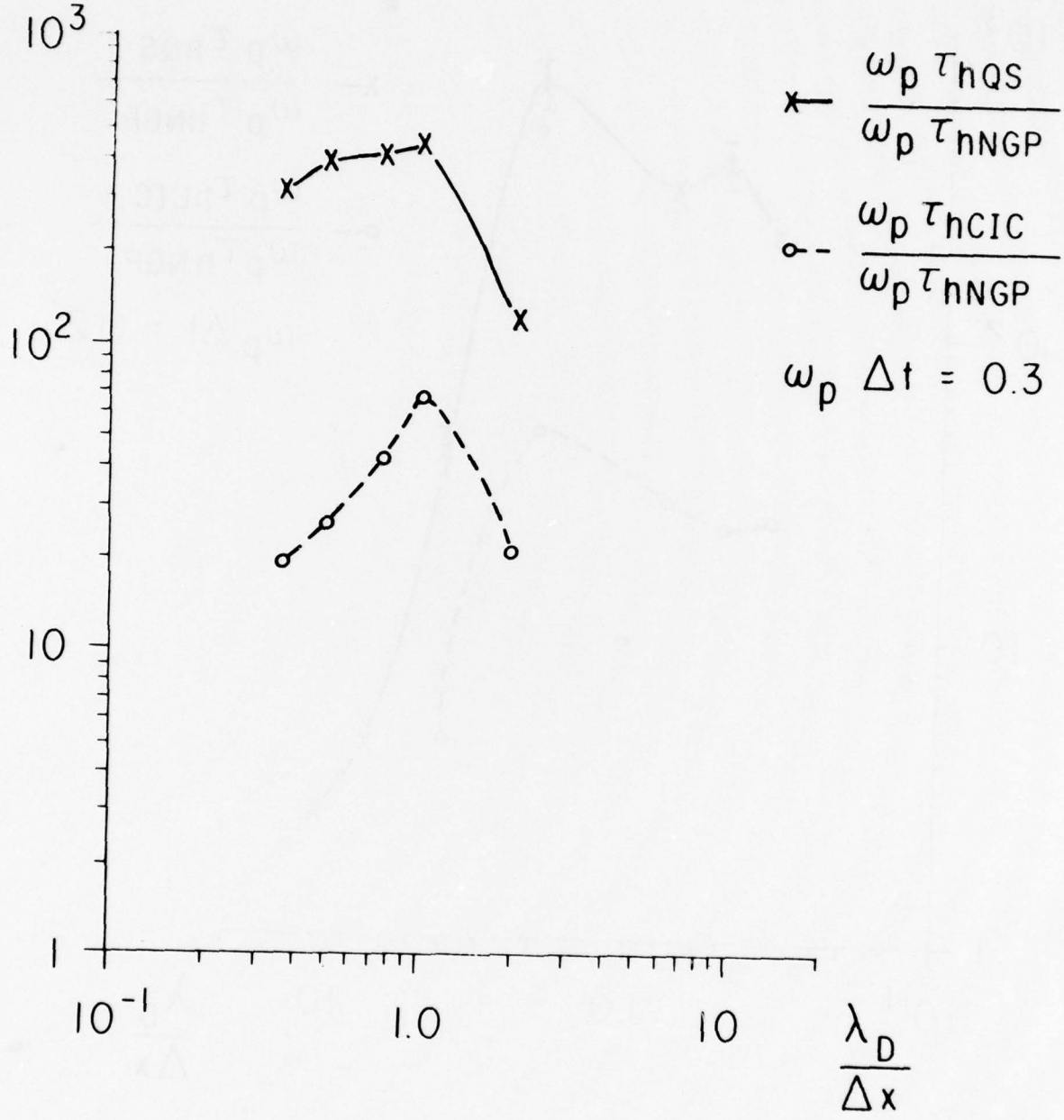

FIG. 6 Ratios of self-heating times vs $\lambda_D/\Delta x$ for $\omega_{pe}\Delta t = 0.3$.

T_{NGP} = 5 μsec/particle/time step

T_{CIC} = 11.6 " " "

T_{QS} = 24 " " "

Defining gain of using a higher order weighting scheme as

$$\text{gain} = \frac{\text{increase in self-heating time}}{\text{increase in computer time}}$$

and going through the optimal path, we have gains as in Table 1.

gain \ $\omega_{pe}\Delta t$	0.1	0.2	0.3
CIC/NGP	$\frac{27.5}{2.3} = 11.9$	$\frac{48}{2.3} = 20.8$	$\frac{70}{2.3} = 30.4$
QS/NGP	$\frac{350}{4.8} = 72.9$	$\frac{650}{4.8} = 135.4$	$\frac{440}{4.8} = 91.6$
QS/CIC = (QS/NGP)/(CIC/NGP)	6.1	6.5	3.0

TABLE 1. Gain in going to a higher order algorithm. The ratios inside the table are increase in self-heating times (i.e., reduction in error in energy) over increase in cost (determined on the CDC 7600 MFE computer at LLL).

The self-heating time can be increased considerably by truncation in k-space. Figure 7 shows the self-heating time $\omega_{pe}\tau_h$ vs k_{max}/k_{last} for the different schemes used (keeping everything fixed but varying k_{last} for each scheme). The gain in self-heating time due to k-space truncation is almost proportional to k_{max}/k_{last} for NGP and is close to but not quite proportional to $(k_{max}/k_{laxt})^2$ for CIC and $(k_{max}/k_{last})^3$ for QS. Thus, k-space truncation further increases the gain of CIC/NGP and QS/NGP and QS/CIC. Table 2 shows approximate gains with k-space truncation.

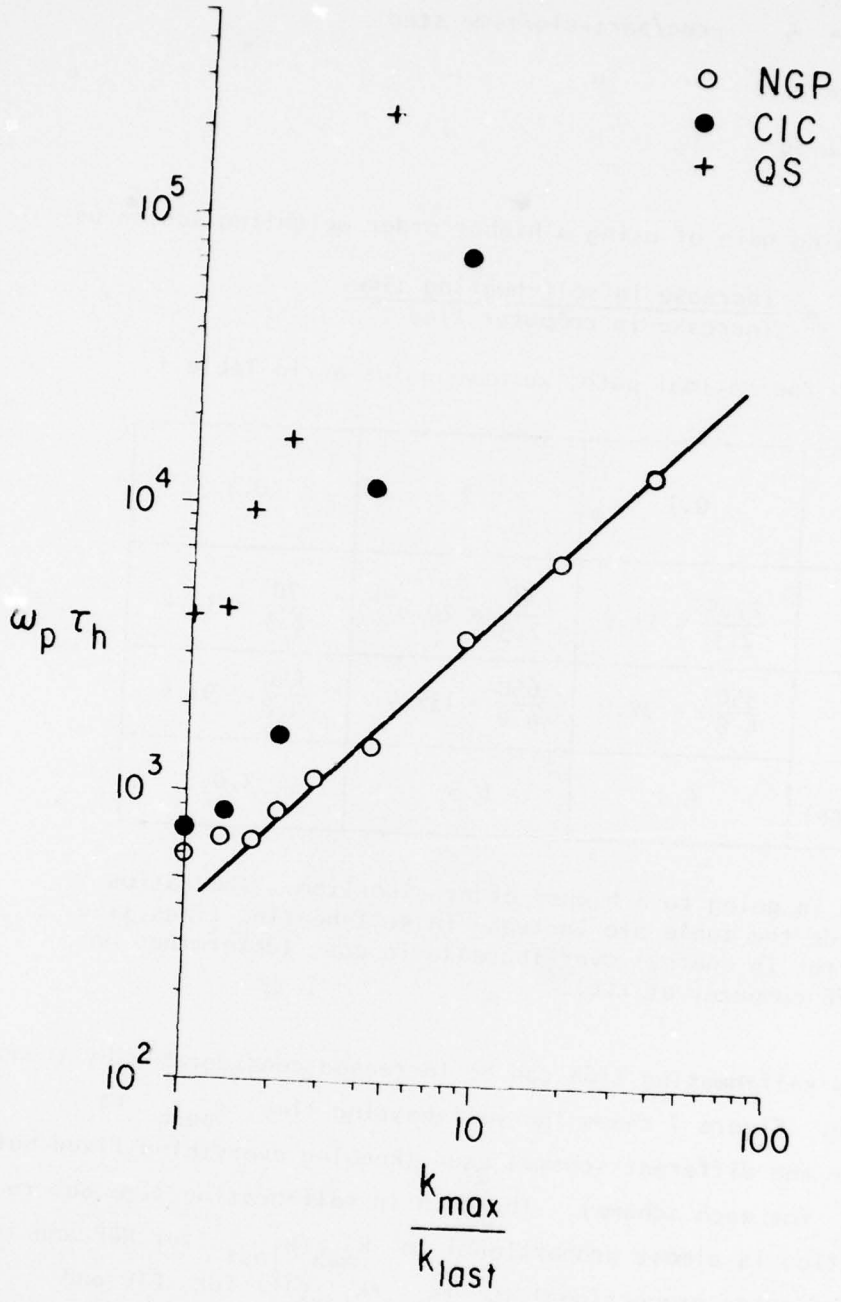

FIG. 7 Self-heating times vs k_{max}/k_{last} for NGP, CIC, QS.

gain \ $\omega_{pe}\Delta t$	0.1	0.2	0.3
CIC/NGP $\times(k_{max}/k_{last})$	11.9	20.8	30.4
QS/NGP $\times(k_{max}/k_{last})^2$	72.9	135.4	91.6
QS/CIC $\times(k_{max}/k_{last})$	6.1	6.5	3.0

TABLE 2. Gain with k-space truncation.

C. VELOCITY-SPACE RING-PLASMA INSTABILITY, MAGNETIZED

J. K. Lee (Prof. C. K. Birdsall)

We have summarized for journal publication our theory and simulations (two papers) on the linear and nonlinear effects of this short-time scale flute-like instability. This instability is unrelated to collisions, resulting from the interactions of energetic ion components (ring-like in velocity-space, but not necessarily monoenergetic) with cooler Maxwellian target ions and electrons. We have included a wide range of electromagnetic effects. A third report on the $1\frac{1}{2}$ dimensional hybrid code (two versions: electrostatic and electromagnetic) will be written separately for submission to the Journal of Computational Physics. The table of contents of the first two papers, including some new results obtained during this quarter, is as follows

VELOCITY-SPACE RING-PLASMA INSTABILITY, MAGNETIZED

PART I: THEORY

PART II: SIMULATIONS

D. ONE-DIMENSIONAL ESI CODE FOR SHEATHS

Yu-Jiuan Chen (Prof. C. K. Birdsall)

There is no new work to report this quarter.

E. PARTICLE TRAJECTORIES IN A CUSP FIELD

Yu-Jiuan Chen (Prof. C. K. Birdsall)

Previous investigation by Levine *et al.*[1] of particle loss in a toroidally symmetric cusp shows a reduction in loss rate due to symmetric geometric effects; this is because the conservation of canonical momentum along the symmetric axis prevents some particles from penetrating (and being lost in) the mirror-like magnetic field at the cusp point. It was pointed out by Boozer and Levine[2] that in a two-dimensional cusp (Fig. 1), a large fraction of the particles in the field-plasma boundary move in definite guiding-center orbits. Therefore, such particles will remain trapped between Coulomb collisions in the absence of microinstabilities. The trapping of particles on the open-cusp field lines is similar to the particle trapping in a mirror machine.

We have re-examined the particle trajectories in an axially symmetric 2d cusp by using Levine's code which integrates Newton's equation of motion using the fourth-order Runge-Kutta method to determine the particle motion in the magnetic field. The magnetic field is given analytically as in Ref. 2. For a sharp boundary, the form is given as

$$\text{(a)}\quad \text{if}\quad x^{2/3} + y^{2/3} < 1 \quad , \quad A_z = B_x = B_y = 0 \qquad (1)$$
$$\text{(b)}\quad \text{if}\quad x^{2/3} + y^{2/3} \geq 1 \quad , \quad z \equiv x + iy$$

[1] Morton A. Levine, Allen H. Boozer, G. Kalman and Pradip Bakshi, "Particle Loss in a Toroidally Symmetric Cusp", Phys. Rev. Lett. 28, 1323 (1972).

[2] Allen H. Boozer and Morton A. Levine, "Particle Trapping in Magnetic Line Cusps", Phys. Rev. Lett. 31, 1287 (1973).

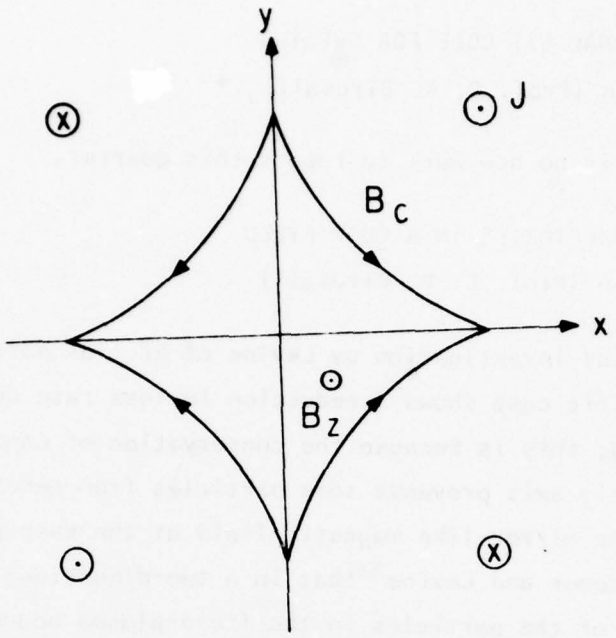

FIG. 1 The configuration of the 2d cusp. $\underline{B}_c$ is the cusp field due to four line current wires. $\underline{B}_z$ is the field perpendicular to the cusp field.

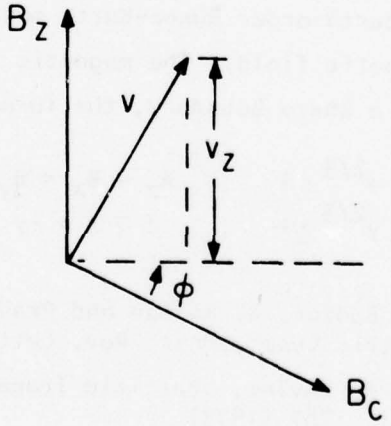

FIG. 2 The coordinates v_z and ϕ on the sphere of possible velocity directions.

$$U \equiv 2[z^2 + (z^4 - 1)^{\frac{1}{2}}]^{1/3}$$

$$L \equiv \tfrac{1}{2}[(U + 4/U) - 4z(U - 4/U)^{-\frac{1}{2}}]$$

$$B \equiv 2/[(U+4/U)^{\frac{1}{2}} - (U+4/U-4L)^{\frac{1}{2}}]$$

$$B_x = \mathrm{Re}(B)$$

$$B_y = -\mathrm{Im}(B)$$

$$A = \mathrm{Im}[3(B^2 + B^{-2})/8] \qquad (2)$$

For a sheath with a finite thickness λ, the vector potential near the plasma is given as

$$A_z(x,y) = B_c[A - \lambda\tanh(A/\lambda)] \qquad (3)$$

The coordinate system used for describing particles is given in Fig. 2. Figure 3(a,b,c,d,e) show the trajectories of particles with various initial conditions. In these calculations, time is measured in inverse cyclotron-frequency units. The sheath thickness, λ, was chosen to be 2.6 times the ion-cyclotron radius, ρ_i, where ρ_i was choosen to be 0.02 times as large as the distance between the center of the plasma and the cusp. The normalized uniform field B_z is $\frac{1}{2}$ and $[B_z^2 + B_c^2]^{\frac{1}{2}} = 1$. The equation of the field-plasma boundary is

$$x^{2/3} + y^{2/3} = 1 \qquad (4)$$

In Fig. 3(a) the guiding center of a particle initially on the boundary at the point (0.356, 0.356) with $v_z/v = 0.4$ and $\phi = 30^\circ$ does not move during the time interval (0.050, 826.437). In Fig. 3(b) the particle initially is at 2 cyclotron radii in the sheath with $v_z/v = 0.6$ and $\phi = 45^\circ$; the guiding center moves down one side then returns. In Fig. 3(c) the particle starts from the cusp point $(1.0, 1.0 \times 10^{-6})$ with $v_z/v = 0.2$ and $\phi = 45^\circ$; it moves up, then circles four sides. Fig. 3(d) shows another type of trajectory in which the particle moves up and only circles one side. In Fig. 3(e) the particle starts from the position (0.396, 0.396), i.e., 3 cyclotron radii from the boundary or 0.4 cyclotron radii outside the sheath, and escapes from the cusp point very quickly.

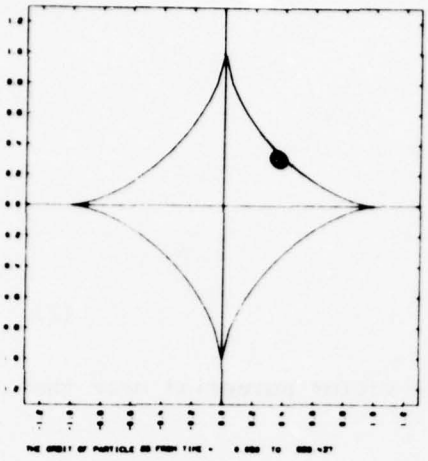

(a)

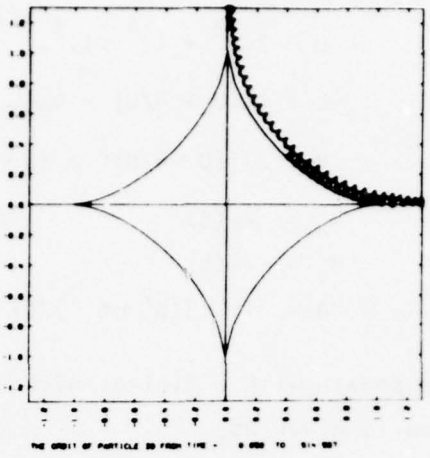

(b)

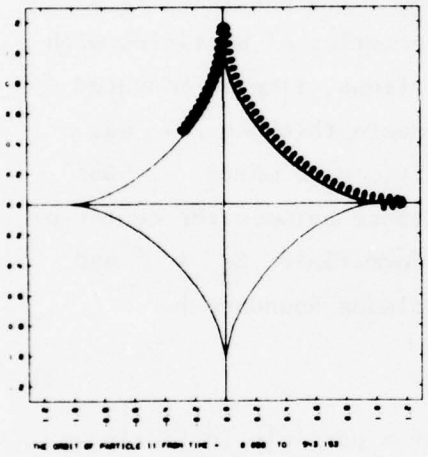

(c)

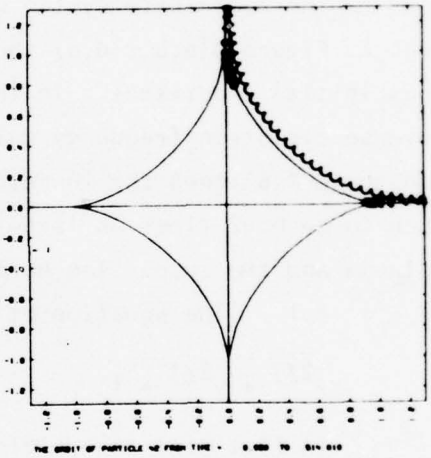

(d)

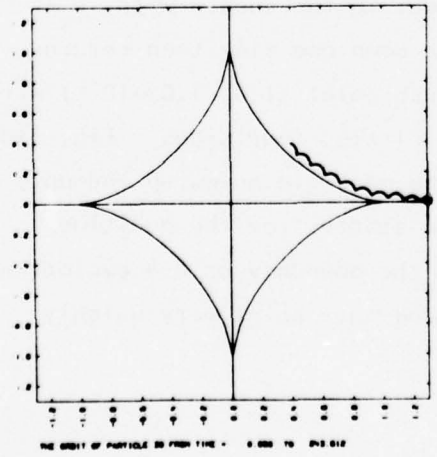

(e)

FIG. 3

These figures show that particles in the sheath move in definite guiding center orbits even though the magnetic field has large variations in magnitude and direction in the sheath. Because the conservation of the canonical momentum,

$$p_z = mv_z + \frac{eA_z}{c} \quad , \tag{5}$$

due to the geometric symmetry and the small spatial variation of Az in the sheath, the trapped particles always remain within a few cyclotron radii of the plasma.

In Fig. 3(c) the axis of the trajectory is shifted slightly to the right in the second quadrant. This shift raises questions about the possible jumps in the usual adiabatic invariants

$$J = \int p_\perp dx_\perp \quad , \tag{6}$$

(where $p_\perp$ and $x_\perp$ are the components of momentum and position vectors perpendicular to the total magnetic field), the magnetic moment μ, and the conserved canonical momentum p_z. These questions will be addressed in the next quarter. Also, the code TIBRO-X will be used to study the particle orbits in either the analytic magnetic field or the self-consistent field with the toroidal effect.

F. PLASMAS WITH FIELD REVERSAL

Douglas Harned (Prof. C. K. Birdsall)

At the present time there is a great deal of interest in field reversed configurations for plasma confinement, partly because of their attractiveness for potential fusion reactor designs as well as for understanding space plasmas (e.g., the bow shock). Before beginning work in the area of field reversal, it has been necessary to determine the status and direction of current research in this area. Of particular laboratory interest are field reversed mirrors and intense ion rings.

Research involving the field reversed mirror has been aimed at calculating electron return currents and the effects of quadrupole fields. The work with quadrupole fields has been approached largely by drawing analogies with the RECE-Berta electron ring experiments at Cornell. Analytic and simulation studies are in progress at Livermore on enhanced resonant diffusion due to the application of a quadrupole field. These results have so far given only very rough agreement with RECE-Berta. The study of quadrupole fields is now being applied to the field reversed mirror by their inclusion in simulations using both TIBRO and SUPERLAYER for single particle trajectories.

With regard to electron return currents, it is still uncertain as to whether or not these currents can effectively prevent the achievement of field reversal. Work by Baldwin and Fowler[1] demonstrates the need for some process (e.g., Ohkawa currents) to prevent neutralization of the current at the field null. SUPERLAYER, which heretofore has ignored electron effects, is now being modified to enable the investigation of electron return currents.

In other areas, concerning FRM, stability analyses have shown that, in order to avoid MHD and tearing modes, the axial length of the plasma as well as the major and minor radii of the field reversed region must be on the order of a few Larmor radii. In the area of transport, very little, if any, work has been done relating to field reversed plasmas.

At Cornell, ion rings have been investigated (through both simulation and theory) from the standpoints of both macro- and micro-instabilities. These studies have determined that the most stable ring is an intermediate configuration somewhere between a long layer and a bicycle tire. A number of codes have been developed to study ion ring behavior, the most recent of which is a 3-dimensional hybrid code using ring-like superparticles.[2]

[1] D. E. Baldwin, T. K. Fowler, "A Reassessment of the Requirements to Obtain Field Reversal in Mirror Machines", UCID-17691, Dec. 20, 1977.

[2] A. Friedman, R. N. Sudan, J. Denavit, "A Linearized 3-D Hybrid Code for Stability Studies of Field Reversed Ion Rings and Mirror Confinement", Bull. Amer. Phys. Soc. 22, 9, p. 1070, 1977.

Among the potential areas for our research are the following:

1) Utilizing TIBRO-X to investigate particle trajectories in field reversed configurations. Here the interest could focus on two areas:
   a) Trajectory behavior near the reconnection points. It is of interest to see what effect the reconnection points will have on confinement. Although this region of the plasma lends itself well to simple models (such as a reversed current loop about the center of a mirror) it may prove difficult to simulate because finite time steps will be inaccurate near the reconnection points.
   b) Confinement of particles in closed field lines. This simulation requires a much more complex model since the very nature of the closed region depends on a diffuse current. One model is the Hill's vortex, used by Miley.[3] This is a rough approximation to the field reversed mirror. It is not self-consistent but does lend itself to analytic solutions of the particle trajectories.
2) Investigation of electron return currents, particularly looking at effects due to charge separation after injection (as suggested by W. Kunkel).
3) Applicaton of stability codes similar to that of Alex Friedman's 3-d hybrid code,[4] using superparticles, to a field reversed mirror configuration.
4) Study of transport properties (this appears to be a wide open field).

G. PARTICLE ACCELERATION, GAMMA-RAY EMISSION, AND SPARKING IN PULSARS

(see next page thru

Dr. Fawley was a guest in our group. This section consists of excerpts from his recent doctoral dissertation (U.C.).

---

[3] M. Y. Wang, G. H. Miley, "Particle Orbits in Field Reversed Mirrors", CO 0-2218-508, June 6, 1977 (submitted to Nuclear Fusion).

[4] A. Friedman, *op. cit.*

G Particle Acceleration, Gamma-Ray Emission, and Sparking in Pulsars

William Marshall Fawley †

ABSTRACT

A rigorous and self-consistent three dimensional method is developed for the calculation of steady-state acceleration of charged particles in the open magnetosphere of a rotating, magnetized, neutron star. This method, which utilizes the applicability of electrostatic potential theory in the corotating frame well within the light cylinder, succeeds in specifying a unique current from pulsar polar caps when this current is space-charge limited. When field line curvature is neglected, the only electrostatic acceleration that occurs is due to the finite inertia of the beam particles. When curvature is included, three different situations may occur according to the geometry of the system. For the aligned rotator ($\mu \| \Omega$), the effects of field line curvature prevent time-steady, totally non-neutral beam acceleration from the polar cap surface, whereas for the orthogonal rotator ($\mu \perp \Omega$), a time-steady solution does exist with charged particles of both signs being accelerated from different halves of the polar cap. When the magnetic and rotation axes are oblique, half of the polar cap surface acts like the aligned rotator and half like the orthogonal rotator. Above the aligned half, there is an electrostatically trapped plasma, while above the orthogonal half, a space-charge limited beam current is accelerated to large energies.

Various electron-positron pair production mechanisms are studied in §III and it is concluded that only magnetic photoabsorption of beam curvature photons is likely to create a dense pair plasma in the open magnetosphere (unless the stellar surface temperature is significantly greater than 100 eV in which case ion coulomb field photoabsorption of thermal photons may produce a large number of pairs). It is improbable that the inertial acceleration corresponding to the strictly aligned rotator can lead to production of a pair plasma sufficiently dense to break the restrictive condition of totally non-neutral current flow. Oblique rotators whose periods are shorter than 0.15 sec $B_{12}^{8/17}\,(\theta_c/\theta_d)^{22/17}\cos^{6/17}\theta_i$ will have copious pair production along favorably curved field lines. Here B_{12} is the surface magnetic field (assumed dipolar) in units of $4.414\cdot 10^{12}$ gauss, θ_c is the actual polar cap opening angle, θ_d is that expected for a pulsar whose closed magnetosphere extends to the light cylinder, and θ_i is the latitude of μ relative to Ω.

In §IV, numerical calculations are presented for the x- and γ-ray emission expected from space-charge limited pulsar models, both with and without pair creation-limited potential drops. The results suggest that some of the COS-B localized γ-ray sources may be "pairless" pulsars. A curvature-induced acceleration model can explain the energetics of the Vela pulsar's γ-ray emission if $\theta_c/\theta_d \approx 2$ and $B \approx 7.\cdot 10^{12}$ gauss but not the double pulse shape or the $\approx 140°$ separation. For the Crab, however, it is not possible to explain the energetics, the 144° main pulse-interpulse separation, or the optical through γ-ray emission spectrum by a surface acceleration model. It thus appears likely that significant particle acceleration must occur at large altitudes ($\gtrsim 10^7$ cm) in the Crab pulsar.

In §V, an analytical solution is given for the initial growth in time and space of an electron-positron spark discharge. Such discharges may occur above ion-emitting polar cap regions and within "outer gaps". These discharges can be sources of coherent low frequency [O(MHz)] radiation in quantities as large as 10^{36} ergs per spark in $\approx 10^{-5}$ seconds (Crab pulsar parameters). Finally, in §VI, the initial results of an electrostatic simulation of a growing spark is presented. These numerical results confirm the analytical hypothesis that a spark develops two "flame fronts" after saturation of the background electric field. Between these fronts, which are moving relativistically, is a dense pair plasma with $E \cdot B \approx 0$.

† See previous page.

VI. Numerical Simulations of Spark Growth and Saturation

A. Introduction

In the previous chapter we gave detailed analytical results concerning the predicted growth and eventual saturation of electron-positron discharges in pulsar open magnetospheres. We found that electrostatic and electromagnetic electric fields developed in opposition to the background "vacuum" field. These induced fields eventually prevent spark growth in the center and we predicted that the edges of the spark would become relativistic "flame fronts" burning their way through the electrostatic energy of the open magnetosphere.

After useful discussion with E.T. Scharlemann, J. Arons and C.K. Birdsall, the author decided to construct a numerical simulation of sparking to determine whether the above scenario had any link to reality. There immediately came a choice as to whether to attempt a full electromagnetic treatment or a far simpler electrostatic one. After study of the EM1 code in use at Berkeley and Lawerence Livermore Laboratory, I decided that it would be difficult and extremely time consuming to adapt EM1 to handle time-dependent electric fields that occurred parallel to the current J (as is the situation in sparking). I therefore turned to the electrostatic code ES1, developed by A. B. Langdon and C.K. Birdsall. In the last section of this chapter we discuss the limitations of a purely electrostatic treatment. We do note here, though, that the results of the previous chapter, especially equation (5.45), indicate that the electrostatic "Coulomb" field may often dominate the radiation electric field in sparking phenomena.

We first discuss that nature of ES1, the changes made to it to study sparks, the initial results, and make final remarks concerning future projects for this type of simulation.

B. ES1 and its Adaptation to Pulsar Sparking

ES1 in its normal form is a fast, one-dimensional (actually 1½ D because it handles both v_x and v_y), non-relativistic, electrostatic code written in Fortran. The code alternately numerically integrates the equation of motion and solves Poisson's equation by fast Fourier transform methods for Φ and E. This leapfrog method in acceleration → velocity → displacement has been shown to be stable for this system of differential equations. The particle coordinates in phase space (x,p_x,p_y) are known "exactly" while the electric field and potential are determined on a grid system and interpolated between grid points.

Once initial conditions have been specified, the code simply integrates the equations forward in time. The user may specify through input parameters which diagnostics are to be printed out (*e.g.* phase space densities, $\eta(x)$,$E(x)$, etc.). The one-dimensionality of the code and the use of cloud-in-cell (linear weighting results in each charge being "slab-like" as far as the computer is concerned. The slab shape in x is triangular with width $2\Delta x$, where Δx is the distance between grid points.

i) Electric Field Solution

As has been emphasized throughout this thesis, pulsar electrodynamics are a multi-dimensional problem. Thus, it might seem strange that we plan to work with a 1-spatial dimension code. However, it is important to realize that one can simulate axisymmetric systems, such as infinite cylinder geometries, by changing Poisson's equation from

$$\nabla^2 \Phi = \frac{d^2}{dx^2} \Phi = -4\pi(\eta - \eta_R) \tag{6.1a}$$

to

$$\nabla^2 \Phi = \left(\frac{d^2}{dx^2} - \kappa^2 \right) \Phi = -4\pi(\eta - \eta_R) \tag{6.1b}$$

with $\kappa^2 = 1/a^2$ where a is the effective transverse (*i.e.* radial) scale of the system. Here x is the coordinate along the infinite dimensions of the system. The justification for expression (6.1b) follows from the use of Fourier transform convolution relationships and Green's Theorem.

The Green function for an infinite cylinder of radius $\tilde{\omega}_c$ whose conducting walls are at zero potential is

$$\mathbf{G}(\mathbf{r}, \mathbf{r}') = \frac{4}{\pi \tilde{\omega}_c} \sum_{l=1}^{\infty} \sum_{m=-l}^{m=+l} \frac{\exp\left[-|x - x'| \, j_{ml} / \tilde{\omega}_c \right]}{j_{ml} J_{l+1}^2 (j_{ml})} J_{ml}(\tilde{\omega} j_{ml} / \tilde{\omega}_c) \, J_{ml}(\tilde{\omega}' j_{ml} / \tilde{\omega}_c) \, e^{im(\phi - \phi')} \quad , \tag{6.2}$$

where $\tilde{\omega}_c$ is the polar cap radius and j_{ml} are the zeroes of the Bessel function J_{ml}. Then, the potential $\Phi(x)$ results from convolving the Green function with the effective charge density $\eta(\mathbf{r}') - \eta_R(\mathbf{r}')$. In Fourier space, we therefore have

$$\Phi(k) = \sum_{l=1}^{\infty} \mathbf{G}_l \left[\eta(k) - \eta_R(k) \right]$$

(to obtain $\eta(k)$ and $\eta_R(k)$ we assume that they both go to zero at $\pm\infty$ and are Lesbesgue integrable). We now assume both strict axisymmetry and that $\eta(\mathbf{r}') - \eta_R(\mathbf{r}')$ does not vary in the transverse $\tilde{\omega}$ direction (*i.e.* each charge is disk-like). We also approximate the infinite series by a single term, $\exp -|x - x'|/\tilde{\omega}_c$, whose Fourier transform is $(k^2 + \kappa^2)^{-1}$. Thus,

$$(k^2 + \kappa^2) \, \Phi(k) = +4\pi \left[\eta(k) - \eta_R(k) \right] ,$$

which is exactly equivalent to expression (6.1b). In our adaptation of ES1, κ^2 was set to $\tilde{\omega}_c^{-2}$. The effects of this two dimensionality (and the conducting walls) is to make all electric fields in the **x**-direction due to a point charge decay in x with an exponential scale height of $\tilde{\omega}_c$.

ES1 nominally works with periodic boundary conditions of $\Phi(0) = \Phi(L)$, where L is the length of the system. While in principle it is possible to change these boundary conditions to represent the true situation of $\Phi(L) - \Phi(0) \neq 0$, the author decided it would be computationally expensive to do so. Instead, we made the system sufficiently long that over the entire simulation time, no particles would get within a couple $\tilde{\omega}_c$ of the edge where the boundary conditions will affect the computed induced E-field. With this safety margin, the induced electric fields due to charge separation within the spark will be accurately computed. Most runs were done with $L \geq 16\tilde{\omega}_c$ (see § C and Figures 6-1 and 6-2 for additional justification of this scheme). Rather than introduce a background of immobile "pseudo" electrons or positrons to represent η_R and thus the vacuum electric field, the code was modified to include a constant E_{vac} to the calculated induced electric field. This constant E_{vac} is an approximation of the $(r/R_*)^{-1/2} - 1$ dependence found above ion-zones and beyond null surfaces. Numerically, E_{vac} was set equal to $3\Omega B R_* \theta_c^3 / 16c$.

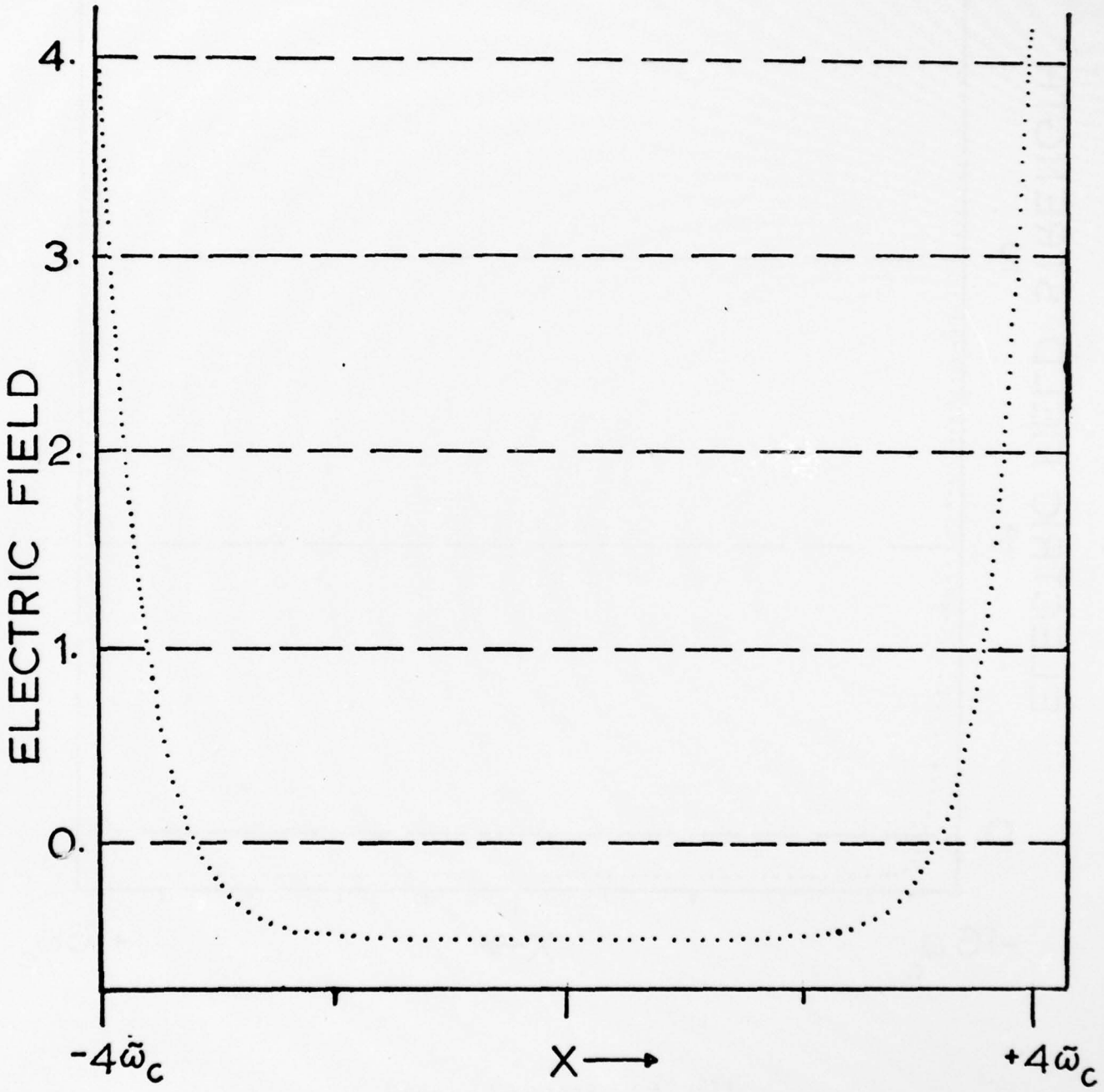

FIG. 6-1 Calculated induced Coulomb electric field for charge density increasing linearly with x and boundary conditions $\Phi(0)=\Phi(L)$. Here $L=8\tilde{\omega}_c$ and one sees that these boundary conditions have little effect on the computed field (in terms of its flatness) beyond $2\tilde{\omega}_c$ from the boundaries.

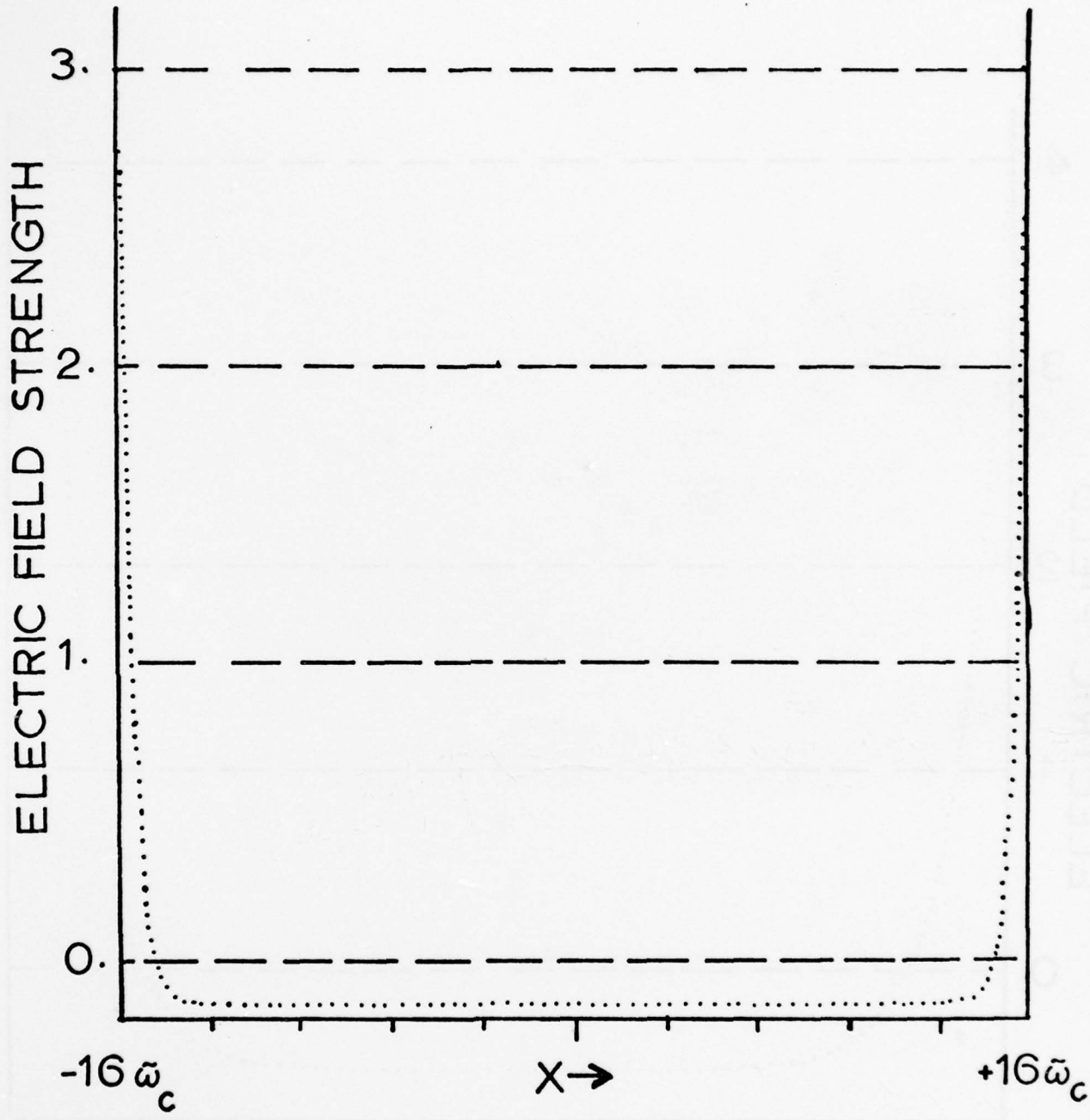

FIG. 6-2 Same as 6-1 but with $L=32\tilde{\omega}_c$.

ii) Equation of Motion and Radiation Reaction

The large particle energies in sparking meant that ES1 had to be changed to a relativistic code. Rather than keep track of particle velocities, one now follows the particle momenta. To compute particle movements during time steps, we set their velocities to $\pm c$ if $|p/mc| \geq 15$ and compute velocities exactly for $|p/mc| < 15$. In general, only an extremely small fraction of the particles have momenta below this limit so that the CPU time required for the momentum → velocity conversion is minimal.

The electrons and positrons follow curved paths and will suffer energy losses via curvature radiation. At the time of this writing, the following scheme was used to include the effects of this braking. The radius of curvature ρ is assumed to be constant with x and set equal to $4R_*/3\theta_c$. The particle momentum is integrated forward in time:

$$p^{\circ}_{new} = p_{old} + \frac{eE}{mc} \tag{6.3}$$

where p is the momentum measured in units of mc. Then two new quantities are computed:

$$p_{new}' = \left([p^{\circ}_{new}]^{-3} + \frac{2e^2 \Delta t}{mc\rho^2} \right)^{-1/3} \tag{6.4a}$$

$$p^{\shortparallel}_{new} = \left([p^{\circ}_{new}]^{-4} + \frac{2e}{3E\rho^2} \right)^{-1/4} \tag{6.4b}$$

$$p_{new} = \max \left(p_{new}', p^{\shortparallel}_{new} \right) \tag{6.4c}$$

The quantity $(p^{\circ}_{new} - p_{new}')$ represents the energy lost in a time interval Δt by a particle coasting along the curved magnetic field. The second quantity, $P^{\shortparallel}_{new}$ approximately represents a particle's radiation reaction-limited momentum in a constant electric field. This approximation is quite good (see Figure 6-3). By taking the maximum of p_{new}' and $p^{\shortparallel}_{new}$, we insist that a particle cannot radiate any more energy than it would in reality in a time interval Δt. This prevents a particle which enters a region of low electric field from suddenly being artificially forced to a low "radiation reaction-limited" energy.

iii) Pair Creation

Sufficiently energetic curvature photons will be absorbed by the magnetic field to form electron-positron pairs. In our adaptation of ES1, we assumed a monochromatic emission spectrum at the critical photon energy of

$$\epsilon mc^2 = 3\Gamma^3 \hbar\, c\rho^{-1} \tag{6.5}$$

and a photon emission rate of

$$\frac{dN_\epsilon}{dt} = \frac{2}{9}\frac{\Gamma c}{\rho}\frac{e^2}{\hbar c}. \tag{6.6}$$

If the photon energy computed in (6.5) is too low for absorption to occur in a distance $\lambda \approx 2\bar{\omega}_c$, then pair creation was ignored for the particle in question. (In reality, pair creation is possible for a distance $\lambda \approx r/3$; thus the spark spreads outwards in x faster than either our numerical treatment or the analytical approach of the previous chapter would predict).

An "on-the-spot" approximation was made to pair creation when it did occur; *i.e.* the pair was created at virtually the same position as its parent particle. In the latest version of ES1-SPARK, we take into account the "reversing" effects of the electric field. Thus, one species is created at the same position as the parent particle while the other species has an average lag of $\delta x \approx c\Delta t/2$. Each newly created particle is given an initial momentum of

$$p_{pair} = \alpha \frac{p_{new} - p^{o}_{new}}{2\dfrac{dN_\epsilon}{dt}\Delta t} \tag{6.7}$$

where $\alpha \leqslant 1$ takes into account the small pitch angle synchrotron losses of the newly created pair.

We also instituted a cutoff to the pair creation rate such that no more than eight pairs per particle could be created per time step. This cutoff is only needed when instabilities such as $\omega_p \Delta t \rightarrow O(1)$ threaten to prevent a simulation from finishing due to exponential blowups. One can normally tell when this blowup occurs from the output diagnostics (*i.e.* the pair creation rate suddenly hits the maximum of eight particles per time step and the plasma frequency begins climbing exponentially in the saturation regime).

ES1 normally handles a constant number of particles. The growth in our particle number due to pair creation meant that another change had to be made. This was to introduce the routine "SQUEEZ" which squeezes the particle number down by an arbitrary factor (in our case three was chosen). Most of our runs were done with a maximum number of 2500 electrons and positrons to be held in memory. When this number was exceeded, SQUEEZ was called and it randomly threw away two-thirds of the particles. The remaining third had their charge and mass increased by a factor of three. Thus, both the charge density and plasma frequency remained unchanged, save for the random fluctuations due to the non-continuous distribution of $\approx$800 particles in 64-128 grid cells. No problems were encountered in using this method. Its CPU time is relatively short as it involves only one "do-loop" and *no* computation (just reshuffling of the momenta and position arrays).

iv) Input and Output Diagnostics

At the time of this writing, ES1-SPARK required the following input: number of grid points(NG), length in polar cap radii(LTUBE), timestep (DT) as a fraction of dx/c, pulsar period(P), magnetic field in gauss(BFIELD), the ratio of θ_c to θ_d(WCAP, normally set to 1), and the charge (in electron charges) of the initial super-electron and super-positron as a fraction of $\theta_c \eta_R dx \tilde{\omega}_c^2$(PERVAL, normally set to $\approx 1 \cdot 10^{-7}$ or less). The code then computes the actual values of $\rho, E_{vac}, \tilde{\omega}_c, L$, dx, and dt used in integration.

ES1 is set up to produce "snapshots" of variables like charge density at user-specified intervals during the running of the code. In our runs, we found it most useful to have frequent snapshots of E and η, and less frequent snapshots of $F(p)$ vs p, $N(e^+)$ vs x, and Φ. At the end of the run, time histories of total particle number, kinetic, electrostatic, drift, and thermal energies are produced.

v) Simplified Flow Chart of ES1-SPARK

a) Compute the induced Coulomb E-field from cloud-in-cell weighting of charge density using Poisson's equation modifed for axisymmetric infinite cylinder geometry. Add the vacuum electric field.

b) Compute the new momenta of particles from equation of motion; include the effects of radiation reaction.

c) Compute pair production; put new particles into momentum and position array.

d) If too many particles to fit in the allocated arrays, call SQUEEZ and reduce particle number.

e) Compute particle velocities and move particles; compute new cloud-in-cell charge density.

f) Print out any required snapshots and go to (a) to begin new cycle.

C. Results

Figures 6-1 and 6-2 illustrate the effects of the $\Phi(0)=\Phi(L)$ boundary conditions on the induced electric field from a charge density linearly increasing with position in the $\hat{x}$ direction. This simulates the increase of η_R with x due to the magnetic field curvature. Defining Δx_{crit} as the distance one must go from the boundary $x=0$ or $x=L$ for $E_{induced}(computed)=1/2 E_{induced}(theoretical)$, we see that $\Delta x/L$ drops from 0.2 at $L=8\tilde{\omega}_c$ to 0.064 at $L=32\tilde{\omega}_c$. The flatness of $E_{induced}(computed)$ in the central region reflects the exponential decay with x of the $\Phi=0$ boundary conditions.

Figure 6-3 plots the kinetic energy versus time of a single particle accelerated from rest by the background electric field. The saturation in energy occurs because of the effects of radiation reaction. The computed asymptotic energy of $3.73 \cdot 10^7$ compares with the theoretical radiation reaction-limited energy of $\Gamma_{rr}=3.90 \cdot 10^7$ [the difference is due to our approximations (6.4a) and (6.4b)].

Figure 6-4 shows the growth of a single spark initiated by a single electron and positron pair created by an external γ-ray. One can see that the growth is initially exponential and turns over to a nearly linear growth rate after electric field saturation (see below). The measured e-folding time of $1.20 \cdot 10^{-7}$ seconds compares favorably with the analytical predicted time of $2.05 \cdot 10^{-7}$ for the chosen parameters ($P=0.0331$, $B=2. \cdot 10^{12}$g, $(\theta_c/\theta_d)=1$, $E_{vac}=1.955E05$

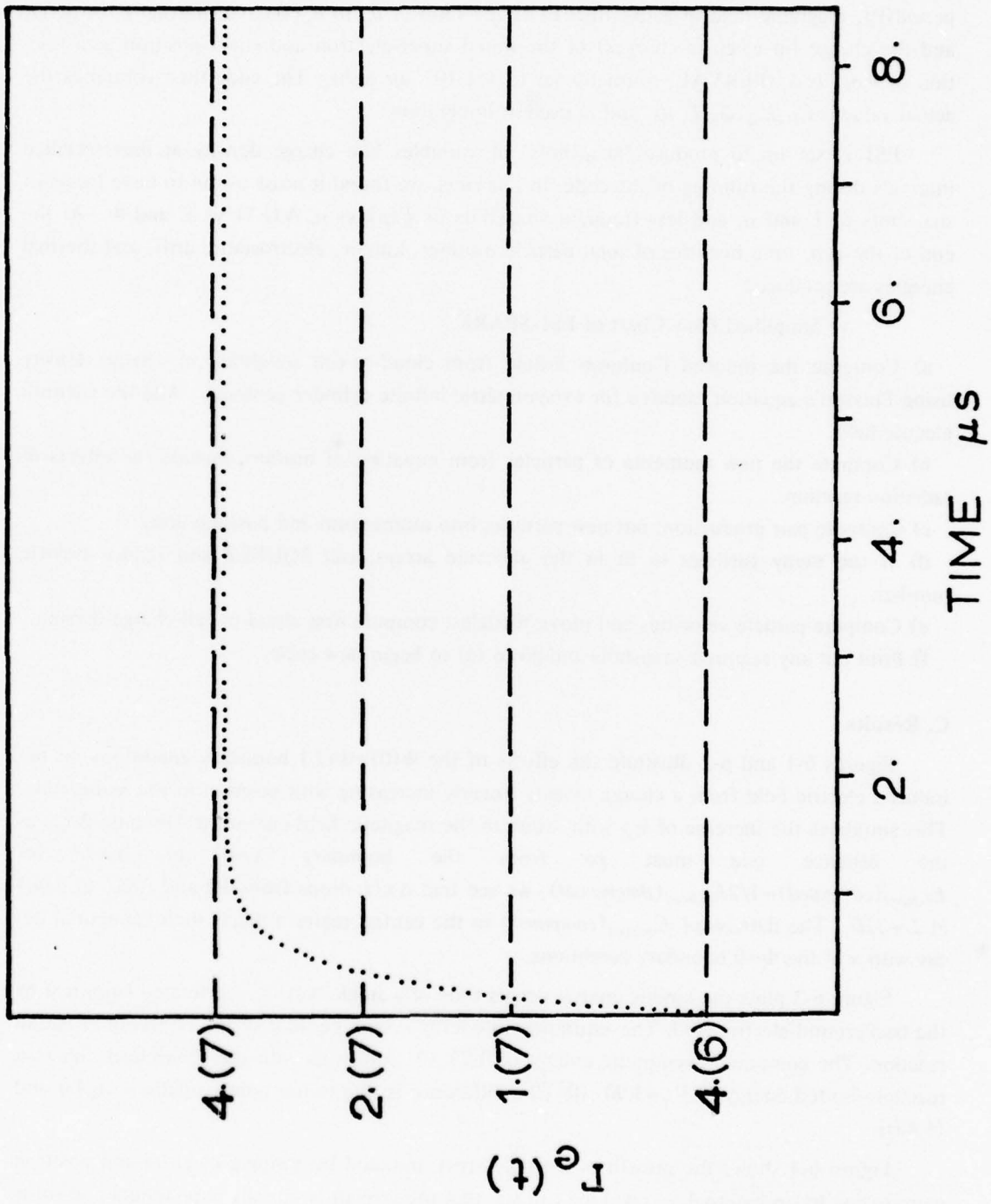

FIG. 6-3 Computed Lorentz factor of an electron starting from rest in a constant electric field as a function of time. Note that the ordinate is a logarithmic scale. The particle obtains a constant asymptotic energy due to radiation reaction along curved field lines.

[machine units], 1.196E06 [statvolts/cm]. The measured rate is somewhat faster because the code permits pair creation by particles before they have obtained radiation reaction-limited energies whereas the analytical results included a forced lag time of $\tau = \Gamma_{\perp}/(eE/mc)$ [*c.f.* equation (5.12)].

We now turn to the most important results of these numerical simulations: what happens in the saturation regime of spark growth?? Figures 6-5 through 6-9 presents various snapshots of the charge density and induced Coulomb electrostatic electric field caused by the relative displacements of the electron and positron densities. One observes that the electric field is growing exponentially in time and, at the center of the spark, is opposed in sign to that of the background vacuum electric field. As one leaves the center and approaches the system boundaries, $E_{induced}$ changes sign. This occurs as one crosses the region of maximum charge density which acts like a surface charge although its thickness is comparable to $\tilde{\omega}_c$ before saturation. Eventually, $E_{induced}(x=L/2) \approx E_{vac}$ and the exponential growth of the spark saturates. This saturated electric field maintains a constant value and "diffuses" outwards from the center with increasing time. The charge density does not approach η_R but instead has $d\eta/dx \approx d\eta_R/dx$ which produces the same effect of $E_{vac}+E_{induced} \rightarrow 0$. This should be expected because the *net* charge density must be zero in the spark and all quantities will be symmetric about $x=L/2$.

As time increases, the center region remains shorted out while the outer regions have the "flame front" structure hypothesized in the last chapter. These fronts are topologically similar to shock waves, *i.e.*, if one transforms to the frame comoving with a front, all quantities appear steady in time. Nearly all the new pairs are created in the flame front regions as shown in Figure 6-10. Since the plasma inside these fronts still has quite high Lorentz factors [$O(10^6)$], a small amount of pair creation continues to occur in the central region. Ignoring the numerical difficulties encountered with an ever-growing number density, the code could run forever until the fronts hit the regions affected by the boundary conditions.

The growing number density and the slowly "cooling" (due to curvature radiation losses) pair plasma lead to the plasma frequency increasing with time. A relativistic hot plasma has an effective $\omega_p \propto n^{1/2}(\Delta\Gamma)^{-1}$ where $\Delta\Gamma$ is the dispersion in the pair plasma's Lorentz factors. Thus, as n increases and $\Delta\Gamma$ decreases, $\omega_p \Delta t$ can approach 1 which presents problems. A non-plasma physicist using this type of numerical code quickly learns to his/her dismay that gross numerical instabilities ensue because the imaginary part of the effective numerical plasma frequency is proportional to the *cube* of $\omega_p \Delta t$. In Figure 6-11, we show the beginning of this instability as shown by its effects upon the induced Coulomb field. To date, the only sure-fire method to postpone this instability while retaining the physics is to decrease the time step Δt. On occasion, the plasma responds to this instability by heating itself up, thus increasing $\Delta\Gamma$, reducing ω_p, and making the instability go away for a few more time steps. But in the end, the instability wins out, particles are accelerated to high energies, more pairs are created, $n^{1/2}$ increases faster than $(\Delta\Gamma)^{-1}$ decreases, and there is utter, complete chaos; the *Götterdämmerung* of a numerical spark.

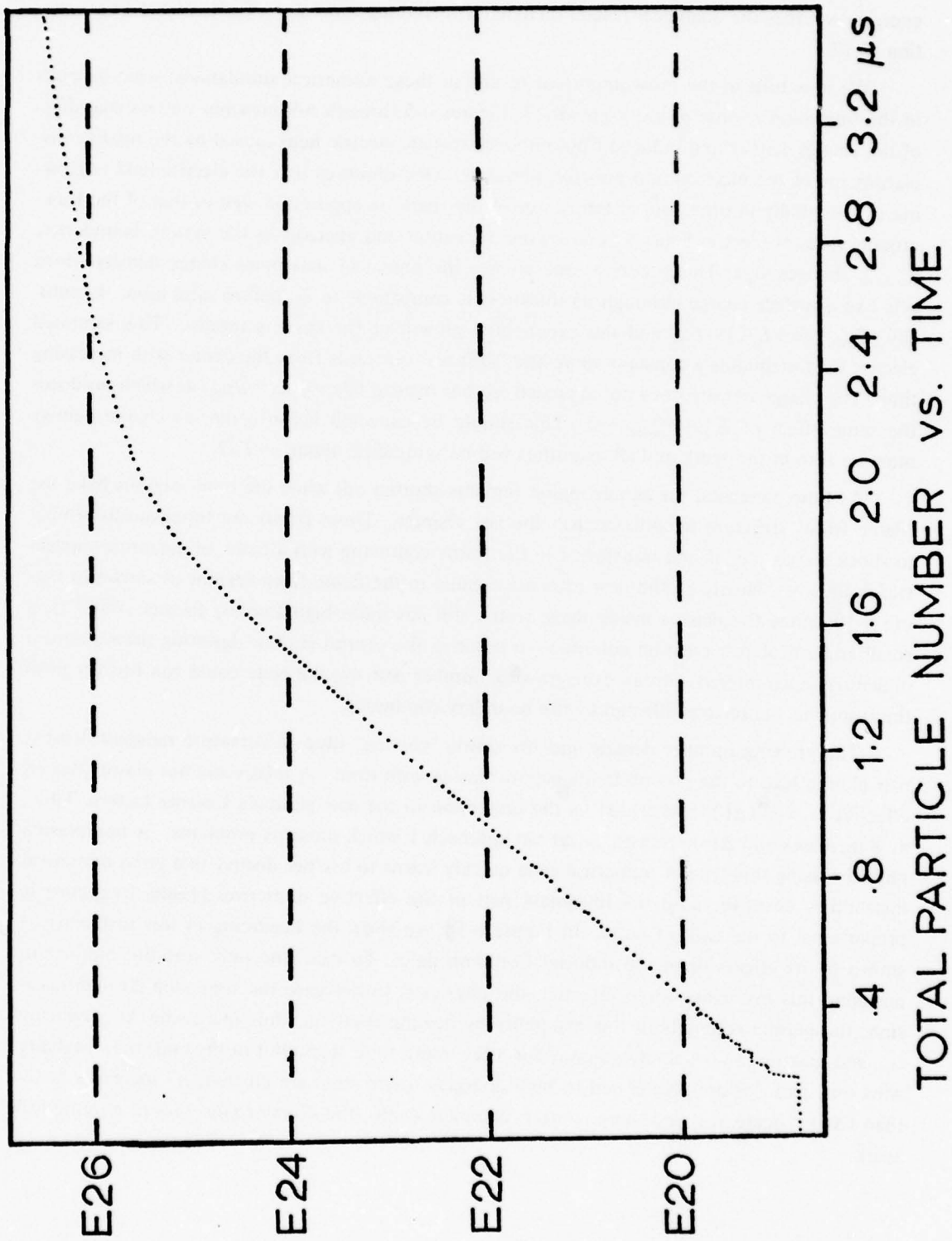

FIG. 6-4 Initial exponential growth in total particle number followed by saturated linear growth of an electron-positron spark discharge.

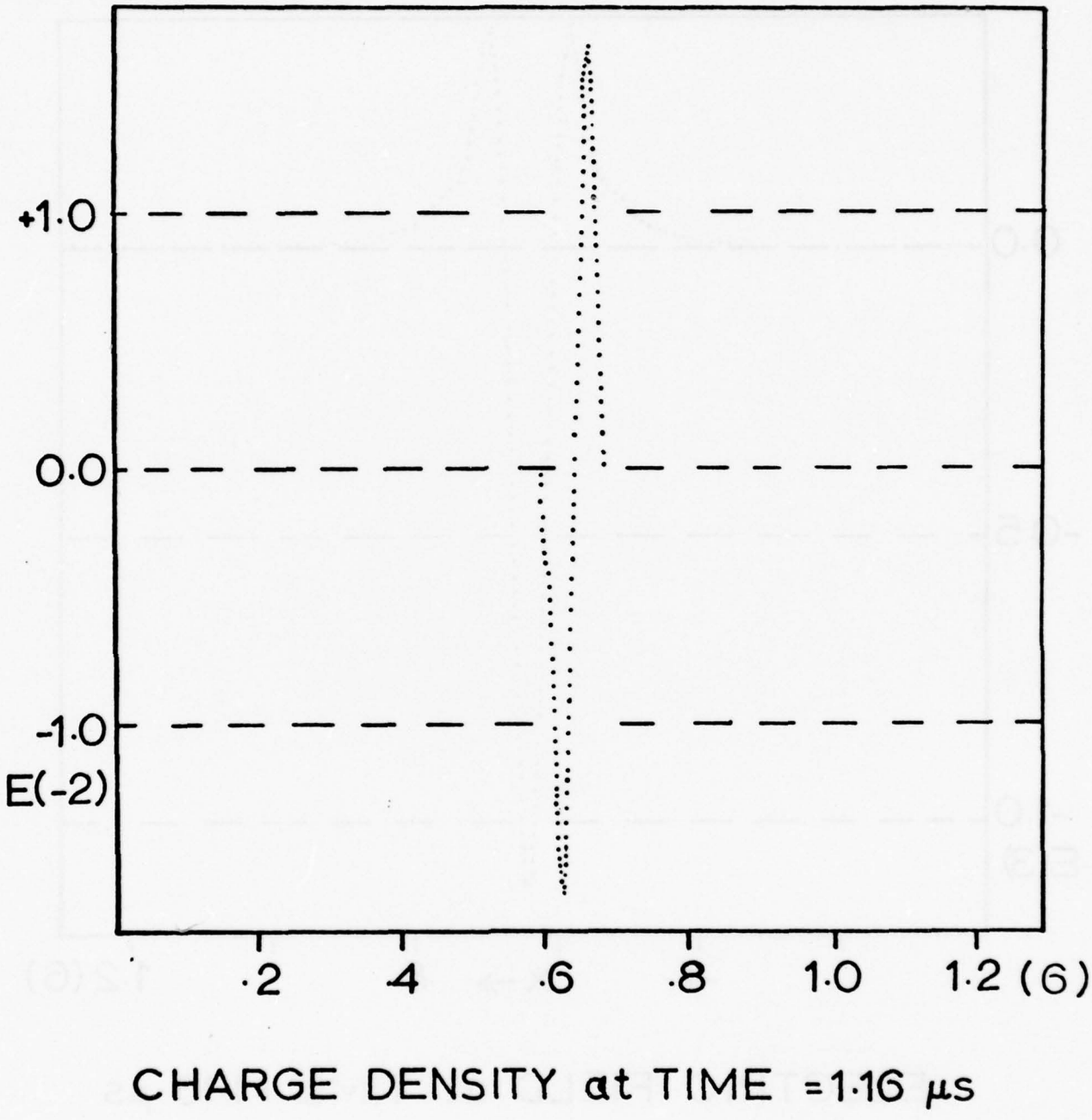

FIG. 6-5 Computed charge density (in machine units) as a function of x after 1.16μs. This is still in the exponential growth regime of the spark. Simulation parameters are P=0.0331 sec, B=2.$\cdot 10^{12}$ gauss, θ_e/θ_d=1, $PERVAL$=1.$\cdot 10^{-7}$, R_*=10^6 cm.

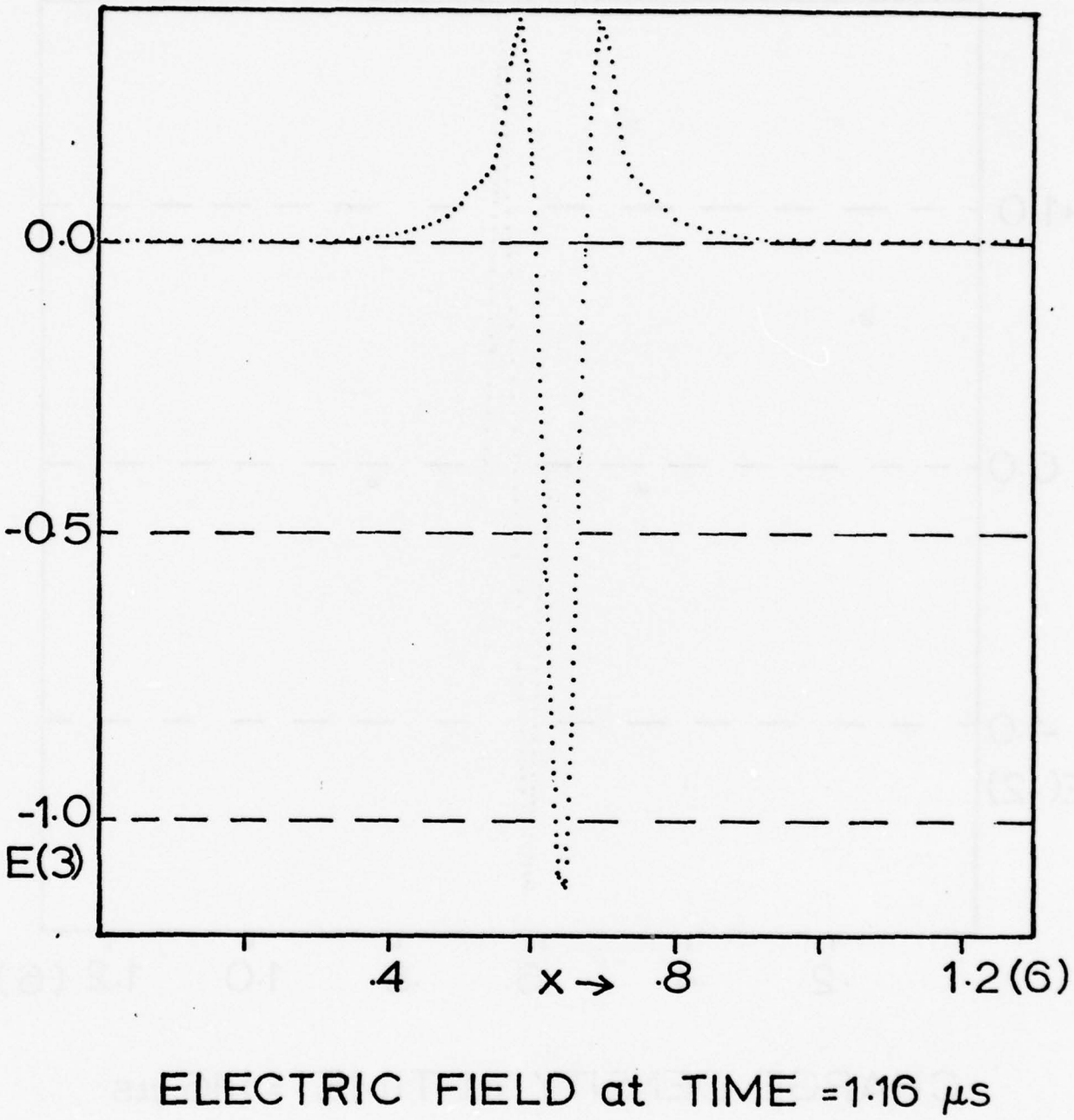

FIG. 6-6,6-7,6-9 Computed electric field (in machine units) due to spark charge density separation. Here the spark has entered the saturated growth regime. The background electric field is $+2.45 \cdot 10^5$. Thus the sum of the induced Coulomb field and the background field is zero.

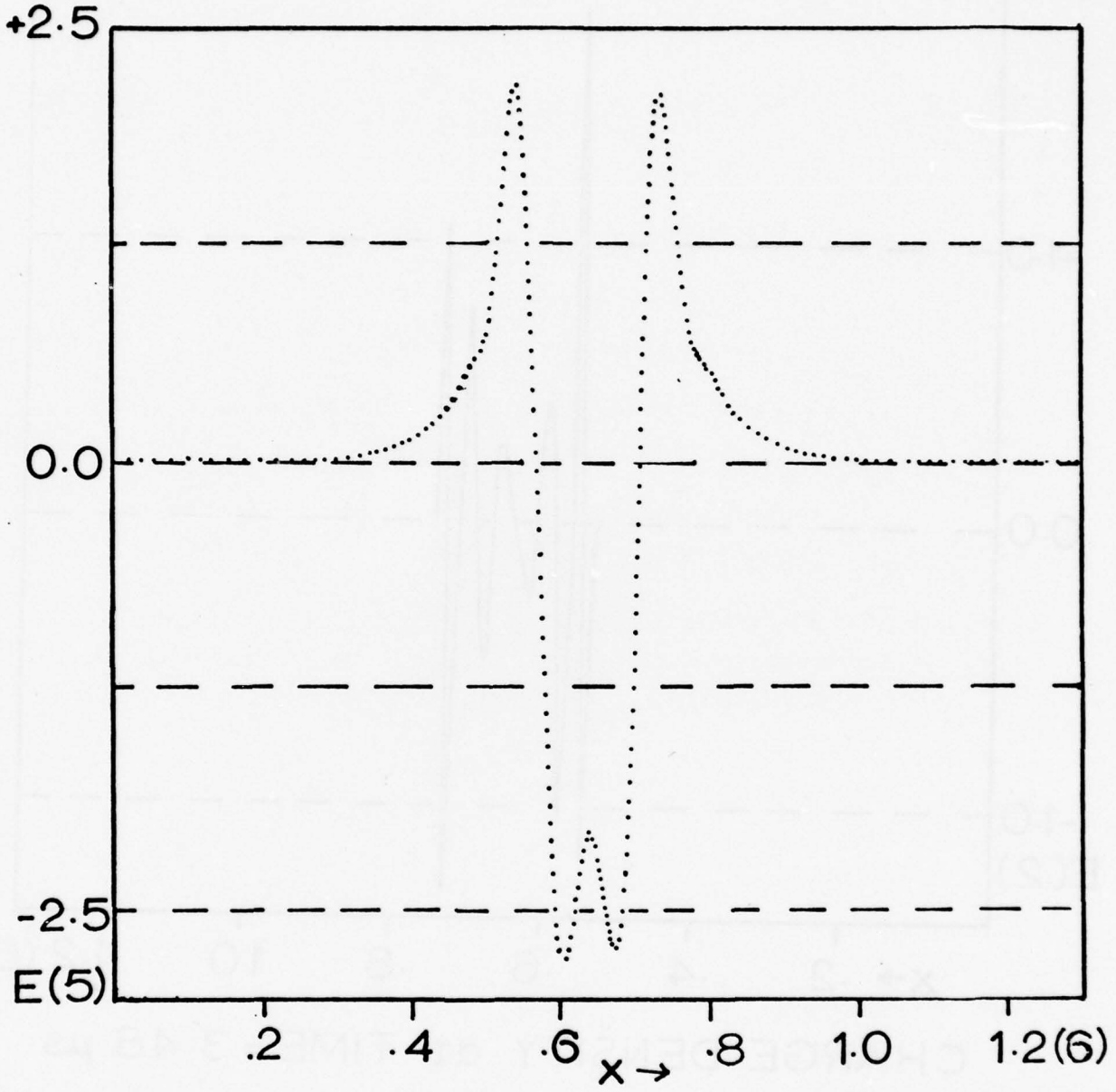

ELECTRIC FIELD at TIME = 2·32 μs

FIG. 6-7

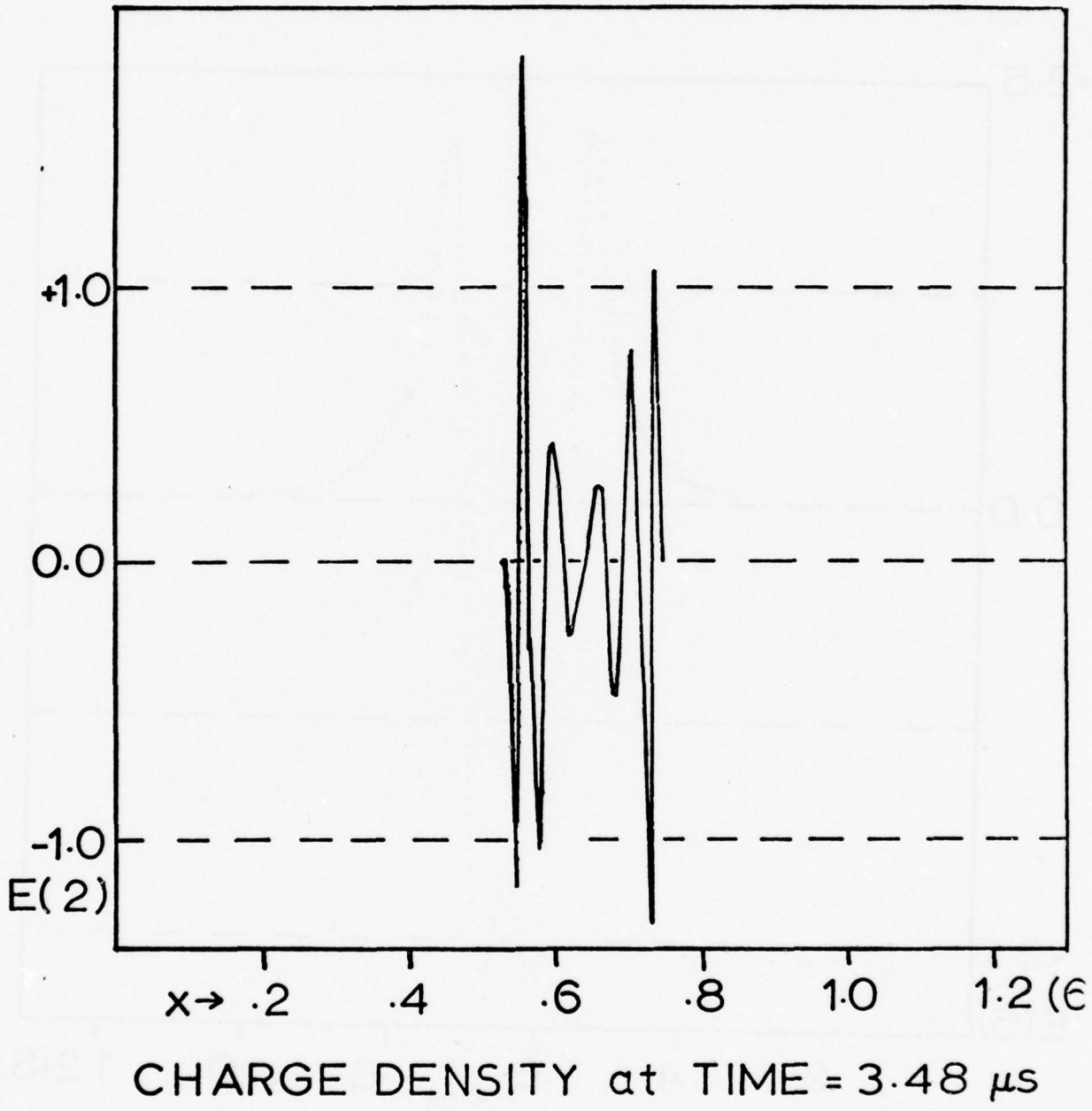

FIG. 6-8 Computed charge density after 3.48μs. This is in the saturated growth regime.

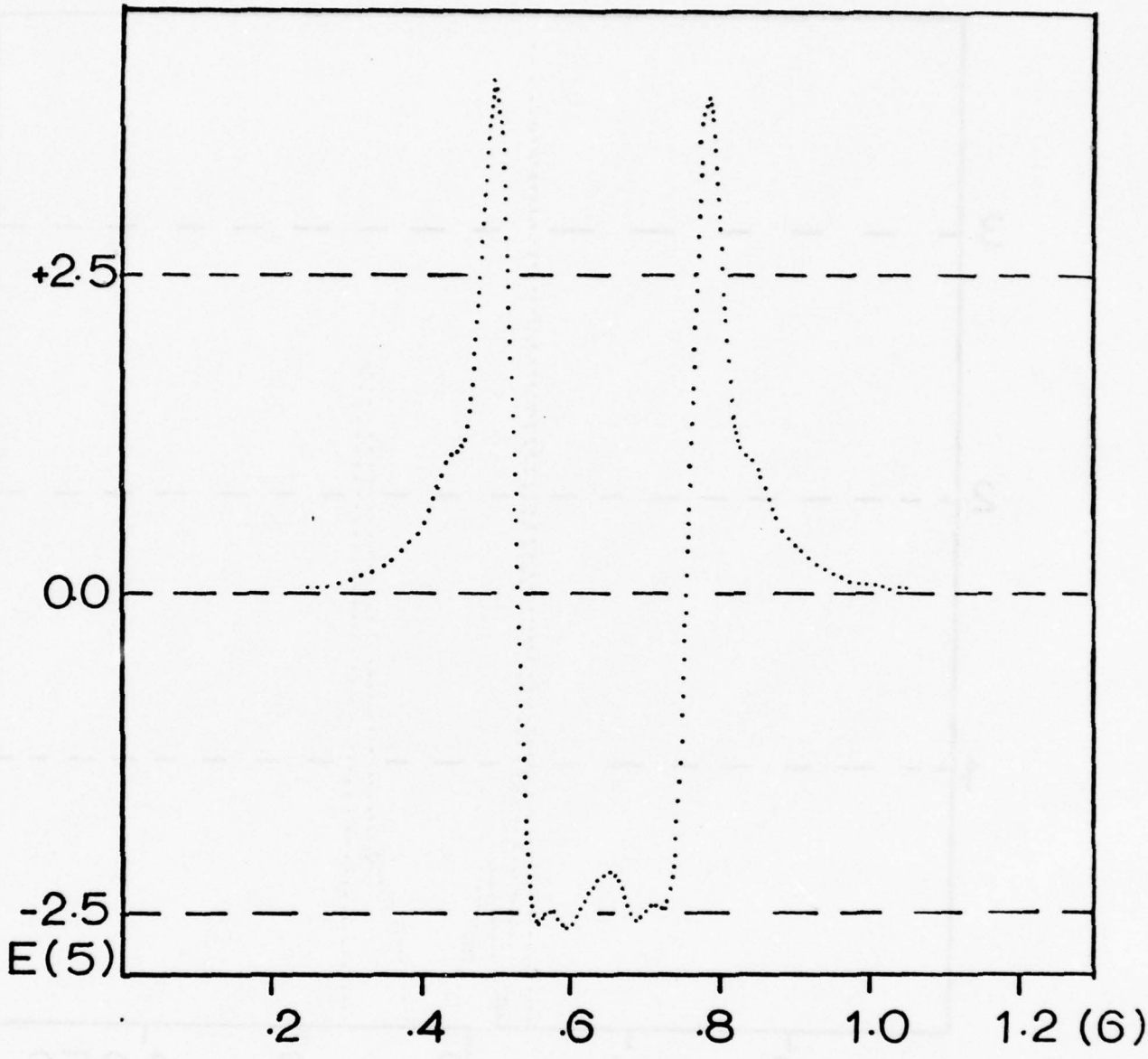

FIG. 6-9

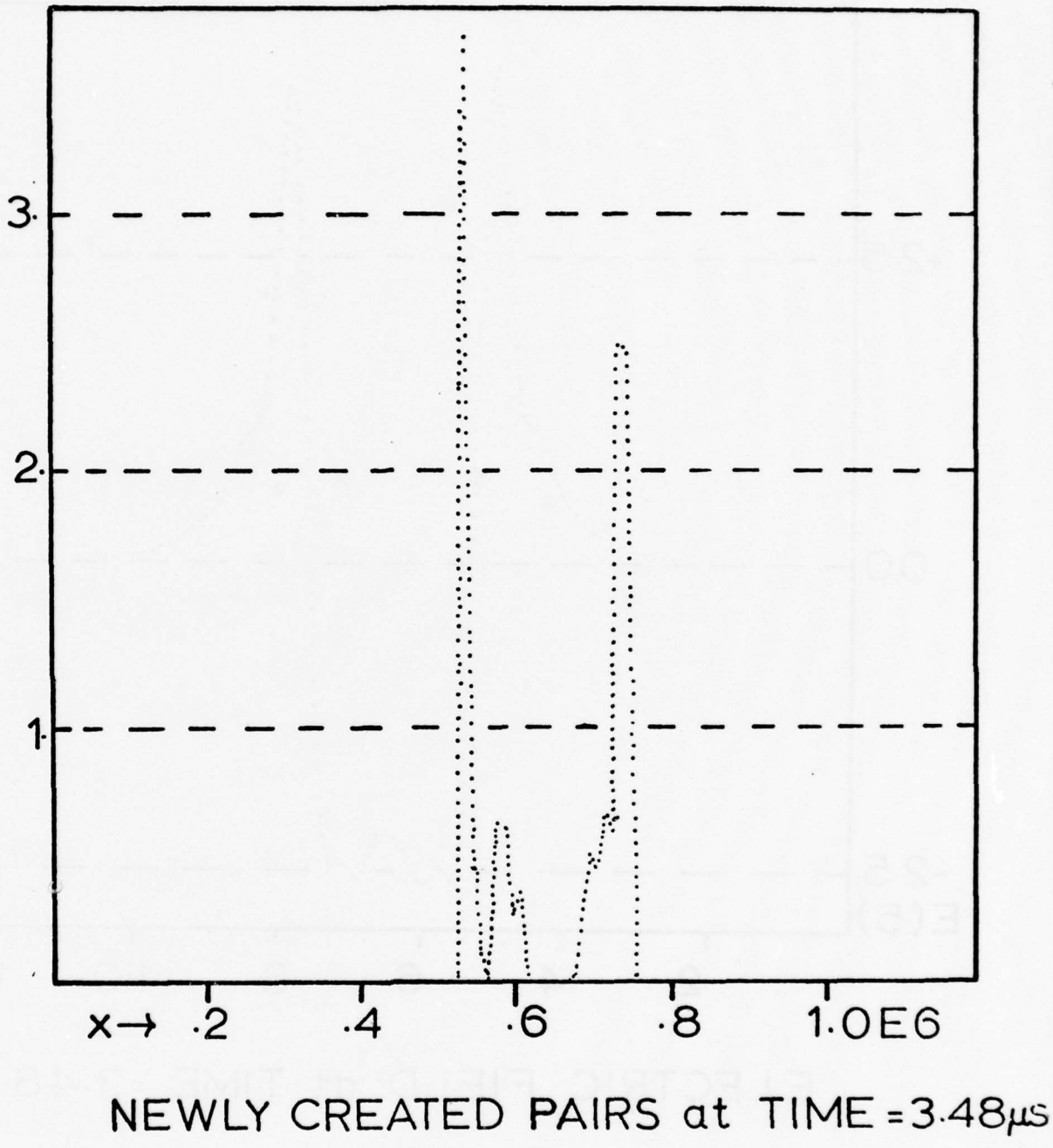

FIG. 6-10 The number density (in arbitrary units) of newly created pairs (in the last time step) plotted against x. Comparison of this figure with Figure 6-9 shows that nearly all the pairs are created at the edge of the spark where $\mathbf{E}\cdot\mathbf{B}$ appreciably departs from zero.

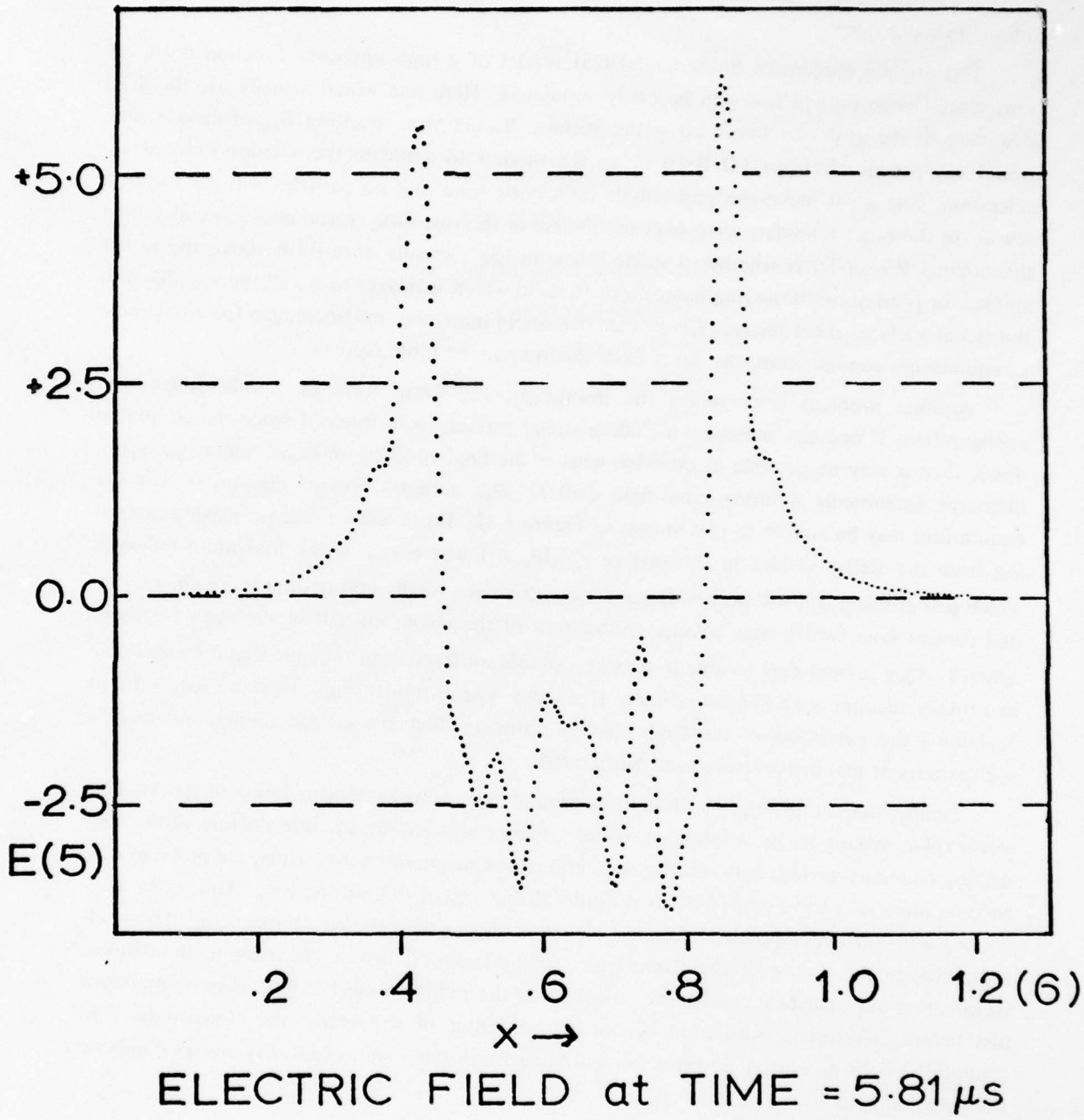

FIG. 6-11 Electric field plotted against x at 5.81μs. Serious numerical instabilities have arisen because the plasma has cooled sufficiently that $\omega_p \Delta t \approx O(1)$.

D. Future Projects in Simulation

There are several additional physical situations that should be simulated besides the infinite cylinder cases.

The original Ruderman Sutherland(1975) model of a high ion work function polar cap *sans* space-charge limited flow can be easily simulated. Here one would actually use the $\Theta=0$ boundary of the grid as a simulated stellar surface. Rather than inserting $E_{\parallel}$ artificially, one would use pseudo-electrons ($\Omega \cdot \mathbf{B}<0$ in an RS model) to simulate the vacuum-induced acceleration. One must make the grid length sufficiently long that no particles will get within a few $\tilde{\omega}_c$ pf the outer boundary $x=L$ over the course of the run. One crucial question concerning the original RS model is whether a stable "vacuum gap" actually does form above the stellar surface, or is an outward moving flame front (behind which η relaxes to η_R all the way down to the stellar surface) more likely? Given that cross-field marching inhibits an gap from obtaining an equilibrium configuration, the flame front picture may be more realistic.

Another problem is to follow the inward moving flame front in a null-surface type configuration. If one can somehow include a stellar surface (with induced space-charge limited flow), then it may be possible to establish what is the final equilibrium of an "outer gap" spark discharge (admittedly ignoring cross-field drifts). The author's present opinion is that the equilibrium may be similar to that shown in Figure 6-12. There will be a dense plasma extending from the stellar surface to the surface $r_{max}(\theta_*, \phi_*)$ where r_{max} is the maximum radius at which pair creation will still occurs. Beyond r_{max}, there is a totally non-neutral space-charge limited current flow (which may balance the current of the $\cos\phi_*>0$ half of the open magnetosphere). This current may be able to extract a significant fraction of the potential drop available in a totally vacuum open magnetosphere. If so, this type of model might be more successful in explaining the energetics of the Crab pulsar's emission than are surface acceleration models such as ours or that of Ruderman and Sutherland.

Finally, the author hopes to do a more accurate electromagnetic simulation of sparks. This will involve making major adaptations to EM1. It may also require the introduction of the conducting boundary surface between the open and closed magnetosphere. Thus, the problem may become more of a wave-guide one. It is doubtful that any of this will be easy. Unless the conducting walls introduce peculiar effects, it would be surprising if the electromagnetic effects radically change the nature of the flame front equilibria found in our electrostatic simulations. Based upon our analytical results, we suspect that the radiation electric field is only important just before electrostatic saturation occurs in the center of the spark; the electrostatic field saturation might be postponed for a few e-folding times but it will eventually always dominate the radiation field.

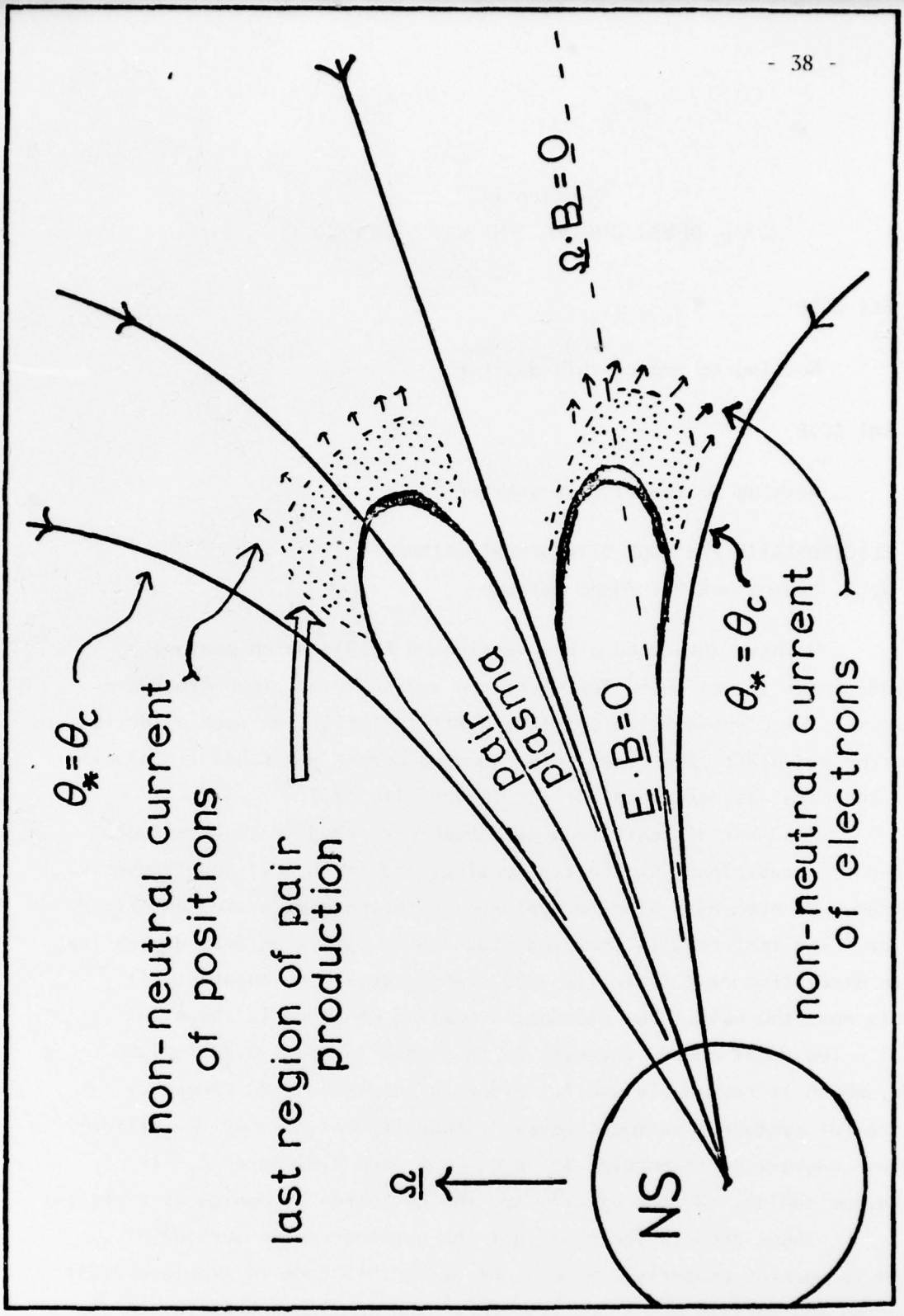

Figure 6-12

FIG. 6-12 Possible equilibrium situation of an $\mu \cdot \Omega < 0$ oblique rotator. Spark discharges occur in both halves of the open magnetosphere. The outward moving flame fronts have stopped at a region where pair creation is barely possible because of the falloff of the background dipolar magnetic field. Beyond this region, there are non-neutral beams of electrons and positrons in the $\cos\phi_* < 0$ and $\cos\phi_* > 0$ regions respectively.

Section III
CODE DEVELOPMENT AND MAINTENANCE

A. ESI CODE

Nothing to report this quarter.

B. EMI CODE

Nothing to report this quarter.

C. ELECTROSTATIC 2½d CODE DEVELOPMENT (EZOHAR)

W. M. Nevins and Dr. Yoshi Matsuda

We have developed a new version of EZOHAR which employs a guiding-center ($\underline{E} \times \underline{B}$) mover for electrons and the usual leap-frog mover for ions. The purpose is to simulate drift instabilities such as drift cyclotron and drift cone modes. The guiding center mover and its algorithm used here was described earlier in QPR III, 1977.

A number of tests runs have been performed to check effects of boundary conditions, stochastic heating, and frequency, and frequency spectrum. We have used a uniform plasma in the bounded system described earlier. The test results show that the density stays uniform during the entire simulation run, typically 1000 steps, causing no apparent ill effects near the wall. The stochastic heating observed is shown in Fig. 1. The total energy increase in this case is about 0.3% in 1000 steps, which is reasonably small. Figure 2 shows measured frequency spectra for cyclotron harmonic waves. These figures are for two different wave numbers corresponding to $k_y \rho_i$ 0.4 and 2.8 where ρ_i is ion Larmor radius. We can clearly see the cyclotron harmonics as expected.

These results indicate that the guiding-center version of EZOHAR is working properly. We will be using this code to simulate drift cyclotron instability and study its linear and nonlinear behavior in the coming quarter.

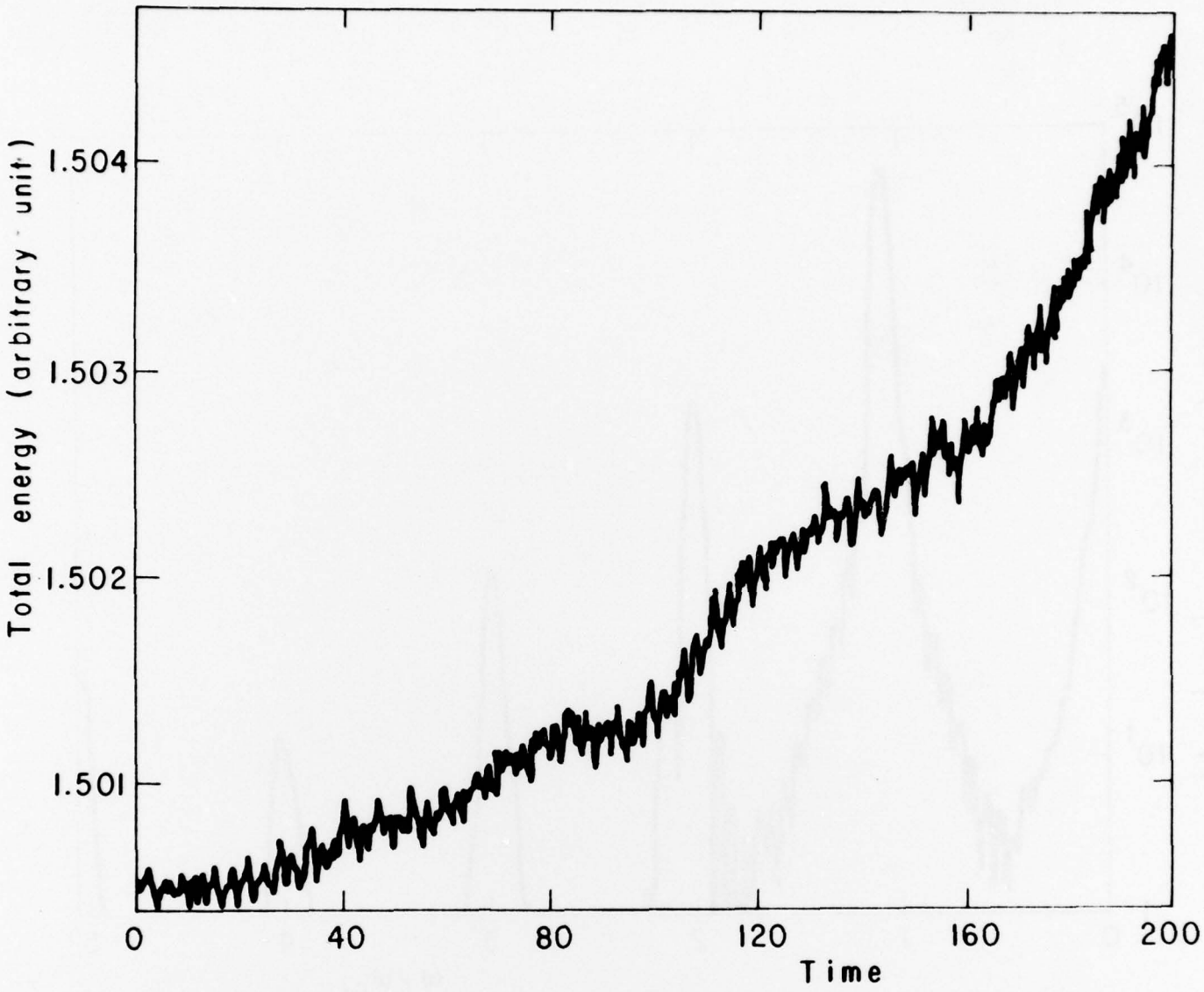

FIG. 1 Total energy vs time in a bounded two-dimensional uniform plasma. Parameters are $N_{ci} = N_{ce} = 4$, $\omega_{ci} = 1$, $\omega_{pi} = 0.5$, $\Delta t = 0.2$.

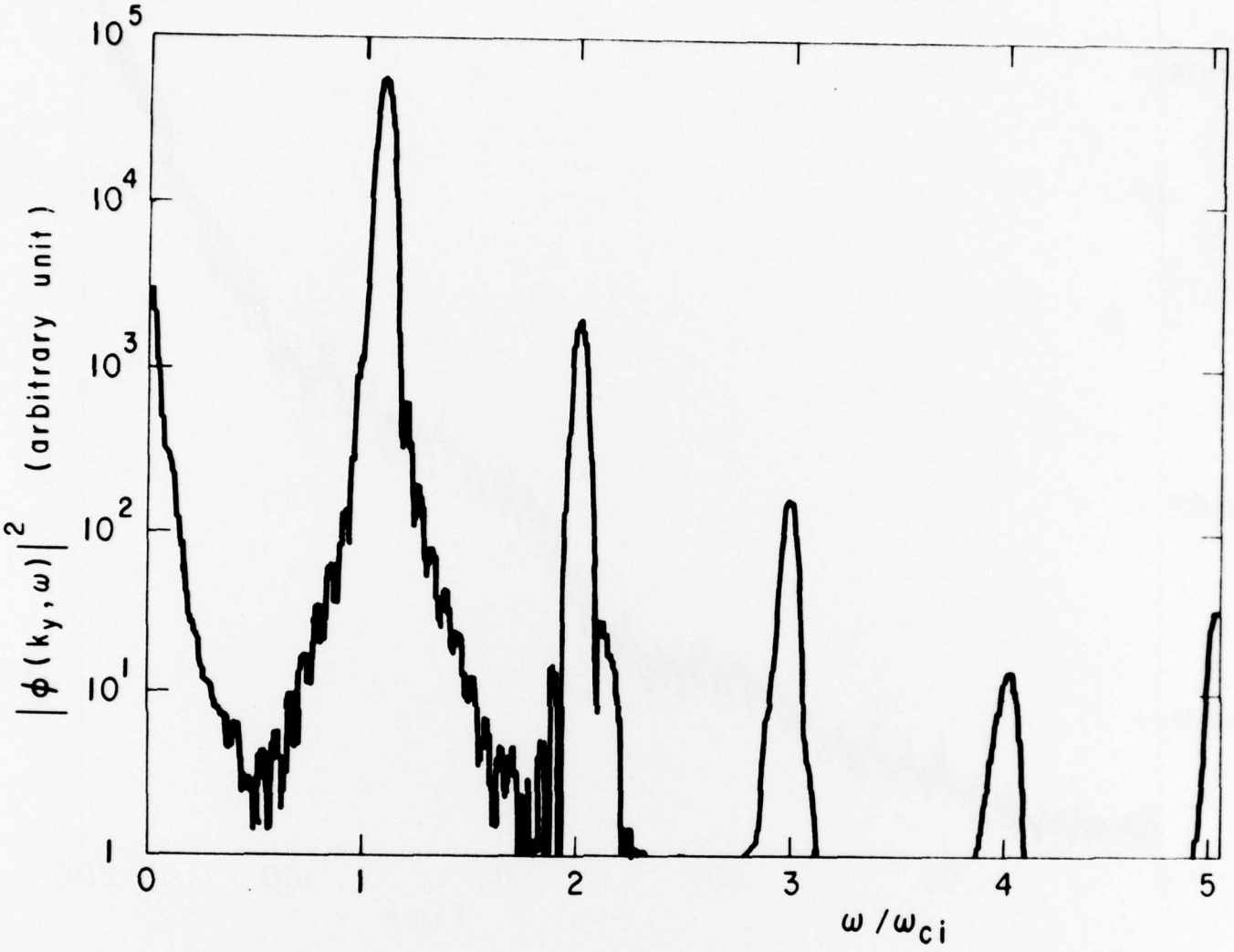

FIG. 2a Frequency spectrum for mode (a) $k_y\rho_i \simeq 0.4$. Parameters are the same as in Fig. 1.

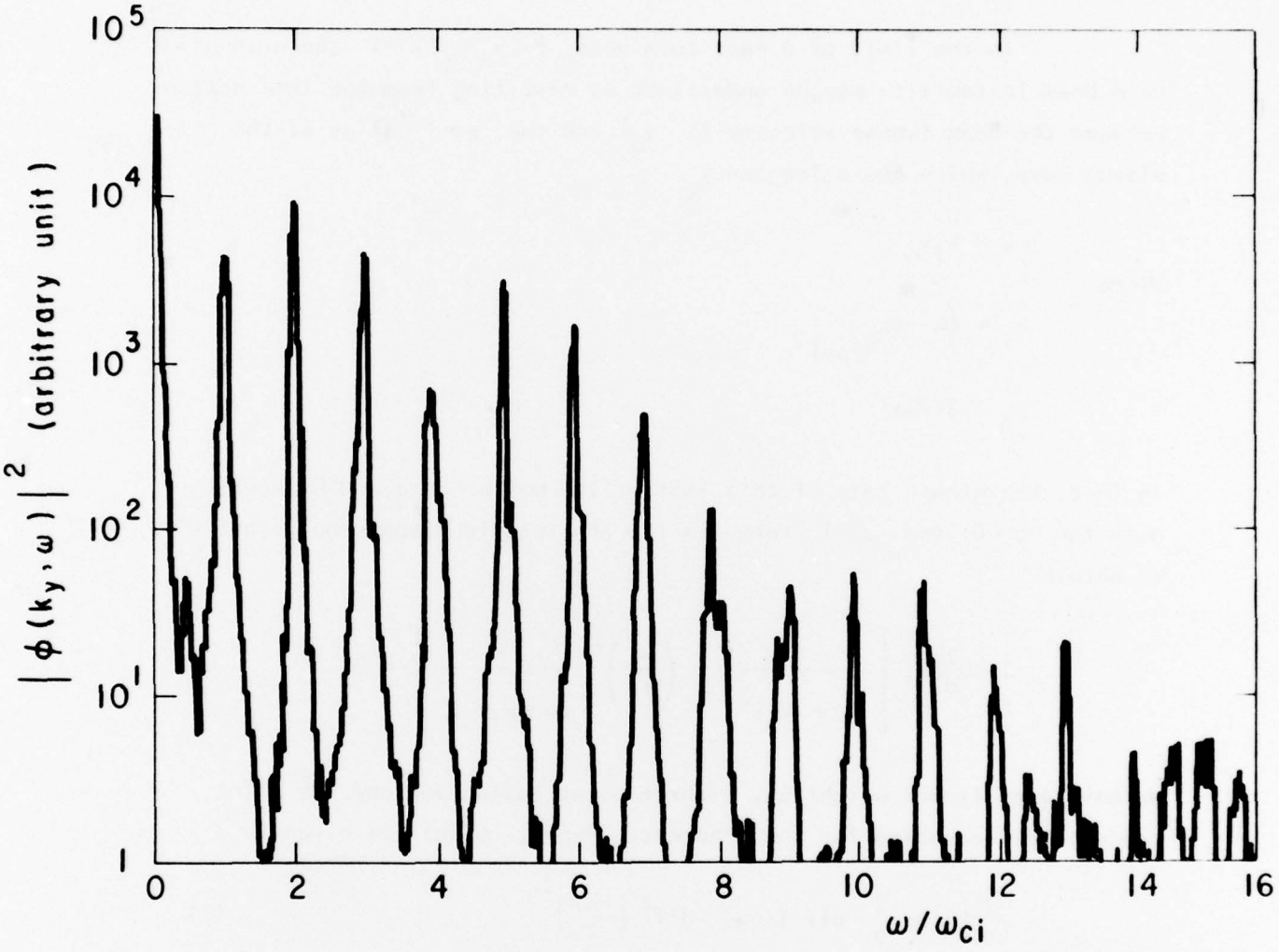

FIG. 2b Frequency spectrum for mode (b) $k_y\rho_i \simeq 2.8$. Parameters are the same as in Fig. 1.

D. THE COLD BEAM INSTABILITY; PREDICTION OF SATURATION LEVEL*

W. M. Nevins and J. Albritton (visiting from Univ. of Rochester, Fall, 1976)

In the limit of a fast cold beam $B \equiv v_o/\omega_p \Delta x \gg 1$ the grid-alias cold beam instability may be understood as resulting from the interaction between the beam (whose velocity is v_o) and the $p = 1$ alias of the plasma wave, which has a frequency

$$\omega = k_1 v_o$$

where

$$k_1 = \left(k - pk_g\right)_{p=1}$$

$$k_g \equiv 2\pi/\Delta x$$

In fact, the growth rate of this instability may be obtained by keeping only the $p = 0$ and $p = 1$ terms in the finite-grid dispersion relation[1] to obtain

$$1 - \omega_p^2(k)\left[\frac{1}{(\omega - kv_o)^2} + \left(\frac{k}{k_1}\right)^3 \frac{1}{(\omega - k_1 v_o)^2}\right] = 0 \qquad (1)$$

We have used linear weighting, a three point Laplacian, and two point centered differencing for the gradient. Hence, $\omega_p^2(k)$ is given by

$$\omega_p^2(k) = \omega_p^2 \ \mathrm{dif}\ (k\Delta x)\ \ \mathrm{dif}^2\left(\frac{k\Delta x}{2}\right) \qquad (2)$$

It is also convenient to define a frequency

$$\Omega \equiv \omega - kv_o \qquad (3)$$

---

*Work done Fall 1976; saved for possible journal note, which has not yet been written. Previous work was a report in our QPR's during 1975, under the title "Cold Beam Instability".

[1] Due to A. B. Langdon, given explicitly in C. K. Birdsall, N. Marion, G. Smith, "Cold Beam Nonphysical Instabilities and Cures", Proc. 7th Conf. on Numerical Simulation of Plasmas, NYU June 2-4 1975. See Eq. (5), p. 178.

Strong coupling between the alias mode and the beam will occur when $\omega/k_1 \simeq v_o$, i.e., when Ω is small. Hence, we consider the limit $\Omega/\omega_p \ll 1$. In addition, we restrict our attention to small values of k, such that $k/k_g \ll 1$, and assume that $k_g v_o/\omega_p \gg 1$. The leading terms in the dispersion relation are then

$$\frac{\Omega^2}{\omega_p^2} \approx \frac{-\zeta^3}{(1-\zeta)^3}\left(1 - \pi^2\zeta^2\right) \tag{4}$$

where

$$\zeta \equiv \frac{k}{k_g}$$

Hence, Ω is purely imaginary for small, positive ζ. The maximum growth rate is determined by choosing ζ to maximize the absolute value of Ω^2. We find

$$\gamma_{max} = 0.2\ \omega_p \tag{6}$$

at

$$\frac{k}{k_g} = 0.4 \tag{7}$$

which agrees with the more complete (more values of p) solutions of Birdsall *et al.*[2]

In this limit (i.e., $k_g v_o/\omega_p \gg 1$), saturation occurs due to the trapping of beam particles in the electric field of the alias wave. This trapping occurs when

$$k_1\delta_1 = 1 \tag{8}$$

where δ_1 is the (Lagrangian) displacement of the beam particles due to the presence of the alias wave.

---

[2]C. K. Birdsall *et al.*, *op. cit.*

We relate the velocity spread of the beam, v_t, to the Lagrangian displacement by the approximation

$$v_t = |\dot{\delta}_1| \simeq |\Omega \delta_1| \tag{9}$$

In writing the second equality, we have used the fact that Ω is the frequency of the alias wave in the reference frame of the beam. Since trapping occurs when $k_1 \delta_1 = 1$, it follows that the beam spread at saturation is given by (approximately)

$$v_t = \left| \frac{\Omega}{k_1} \right| \tag{10}$$

Substituting the appropriate values for the fastest growing mode gives

$$\left(v_t\right)_{\text{saturation}} \simeq 0.05\ \omega_p \Delta x \tag{11}$$

Finally, we note that when the Debye length of the beam is taken to be $\lambda_D = v_t \omega_p$, this result may be written as

$$\frac{\lambda_D}{\Delta x} \simeq 0.05 \tag{12}$$

This is in excellent agreement with the simulation results shown in Fig. 1 on p. 18, QPR II, July 1, 1975. We also note that an examination of the phase space plots at saturation reveals clumping of the beam into vortices with a spacing equal to the wave length of the $p = 1$ alias. Hence, we conclude that this simple trapping model accurately describes the saturation of the grid-alias instability in the limit of a fast cold beam.

Section IV

PLASMA SIMULATION TEXT

No progress this quarter.

Section V

SUMMARY OF REPORTS, TALKS, PUBLICATIONS IN PAST QUARTER

M. J. Gerver, "Radial Normal Mode Calculation of Warm Plasma Stabilization of the Drift Cone Mode", Phys. Fluids 21 3, pp. 443-446, March 1978.

DISTRIBUTION LIST

Contractor (DOE)
Robert Price
Donald Priester
Walter Sadowsky
Glenn Ingram
Oscar Manley

Contractor (ONR)
Padgett (plus 67 to ONR list)

Berkeley Campus
Birdsall, Matsuda, Chen, Peiravi, Harned Lee, Lichtenberg, Lieberman, Arons, McKee, Chorin, Fawley

Berkeley Lab (LBL)
Kunkel, Kaufman, Cooper, Maria Feder (library), Pyle, Berk

Livermore (LLL)
Byers, McNamara, Maron, Kruer, Langdon, Lasinski, Max, Fuss, Bruijnes, Killeen, Marx, Mirin, Fries, Harte, Cohen, Taylor, CTR Library
Briggs, Lee, Chambers, Smith

Israel
Gell, Cuperman

U.C. Davis
DeGroot

Univ. of Maryland
Guillory, Sternlieb

U.C.L.A.
Dawson, Lin

Stanford
Buneman, Barnes

Columbia Univ.
Chu

Princeton PPL
Chen, Okuda. Graydon (Library), Nevins, Tang

Oak Ridge NL
Meier, Dory, Mook (Library)

Los Alamos SL
Lindman, Nielson, Burnett (Library)
Gitomer, Lewis, Hewett, Forslund, Godfrey

Stevens Inst.
Rosen

ITT-Spain
Canosa

U.C.-Irvine
Rynn

NASA
Hohl

Kirtland AF3
Pettus

NOTE: Please send advice on additions/deletions to Prof. C.K. Birdsall. If you want your copy or an additional copy to be sent to your library, please send complete address.

Northwestern Univ.
Denavit

Naval Research Lab
Boris, Winsor, Lee

SAI
Klein, McBride, Wagner, Nicholson

IBM Palo Alto
Gazdag

EPRI
Gough, Scott

General Atomic
Helton, Tommey (Library)

Univ. of Reading
Hockney, Eastwood

Inst. fur Plasmaphysik
Biskamp

Bell Labs
Hasegawa

Culham Lab
Roberts

Plasma Physics Inst. Nagoya
Kamimura

MIT
Bers

NYU
Grad

Univ. of Wisconsin
Shohet

Univ. of Texas
Macmahon, Horton

Univ. of Iowa
Knorr, Joyce

Cornell Univ.
Gerver, Friedman

Univ. Rochester
Albritton

Sandia Laboratories
Freeman, Poukey

Bhabha Atomic Research Centre
R.N. Aiyer

Mission Research Corp
W. E. Hobbs
C. E. Rathmann

Dr. Robert E. Price
Fusion Plasma Theory Branch
Applied Plasma Physics Prgm.
Div. of Magnetic Fusion Energy
ERDA Headquarters
Germantown, Maryland 20767

Mr. Donald Priester
Fusion Plasma Theory Branch
Applied Plasma Physics Prgm.
Div. of Magnetic Fusion Energy
ERDA Headquarters
Germantown, Maryland 20767

Dr. Walter Sadowsky
Fusion Plasma Theory Branch
Applied Plasma Physics Prgm.
Div. of Magnetic Fusion Energy
ERDA Headquarters
Germantown, Maryland 20767

Dr. Glenn Ingram
Fusion Plasma Theory Branch
Applied Plasma Physics Prgm.
Div. of Magnetic Fusion Energy
ERDA Headquarters
Germantown, Maryland 20767

Prof. C.K. Birdsall
EECS Dept. 191M Cory Hall
U.C.B. Campus Mail

Dr. Yoshi Matsuda
EECS Dept. 119ME Cory Hall
U.C.B. Campus Mail

Ali Peiravi
EECS Dept. 119MD Cory Hall
U.C.B. Campus Mail

Dr. William Nevins
PRINCETON UNIVERSITY
Plasma Physics Laboratory
Princeton NJ 08540

Prof. A.J. Lichtenberg
EECS Dept. 185M Cory Hall
U.C.B. Campus Mail

Prof. M.A. Lieberman
EECS Dept. 189M Cory Hall
U.C.B. Campus Mail

Mr. Harry Mynick
c/o Allan Kaufman
Dept. 9209, Bldg.50A-3115
LBL, Campus Mail

Prof. J. Arons
Astronomy, 551 Campbell Hall
U.C.B. Campus Mail

Prof. C.F. McKee
Physics Dept. 461 Birge Hall
U.C.B. Campus Mail

Prof. A. Chorin
Math Dept. 829 Evans
U.C.B. Campus Mail

Prof. Wulf B. Kunkel
135 Bldg. 5, LBL
U.C.B. Campus Mail

Prof. Allan N. Kaufman
3115 Bldg. 50A, LBL
U.C.B. Campus Mail

Dr. Robert J. Pyle
117 Bldg. 5, LBL
U.C.B. Campus Mail

Ms. Maria Feder
Building 50B, Room 4206
LBL Library
U.C.B. Campus Mail

Dr. J.A. Byers
L 439, Bldg. 315, Rm285
LLL, U.C.B. Campus Mail

Dr. Brendan McNamara
L439, Bldg. 315
LLL, U.C.B. Campus Mail

Mr. Neil Maron
L440, Bldg. 315
LLL, U.C.B. Campus Mail

Dr. A. Bruce Langdon
L545, LLL
U.C.B. Campus Mail

Dr. Barbara Lasinski
L545
LLL, U.C.B. Campus Mail

Mr. Dieter Fuss
L318
LLL, U.C.B. Campus Mail

Dr. Herbert Berk
LBL, U.C.B. Campus Mail

Dr. John Killeen
L318

Dr. Kenneth Marx
L318
LLL, U.C.B. Campus Mail

Dr. Arthur Mirin
L318
LLL, U.C.B. Campus Mail

Mr. Robert Fries
L439
LLL, U.C.B. Campus Mail

MFE Library
L440
LLL, U.C.B. Campus Mail

Prof. John S. DeGroot
Applied Science Dept.
223 Walker Hall, U.C. Davis
Davis, California 95616

Prof. John Dawson
Physics Department
UCLA, Los Angeles, Ca. 90024

Dr. Yakov Gell
50/7 Rambam Str.
Beer Sheva
ISRAEL

Dr. Tetsuo Kamimura
Institute for Plasma Physics
Nagoya University
Nagoya, JAPAN

Prof. Oscar Buneman
ERL, Stanford University
Stanford, Ca. 94305

Dr. Chris Barnes
ERL, Stanford University
Stanford, Ca. 94305

Dr. Chia K. Chu
Mechanical Engr. Dept.
Columbia University
New York, New York 10027

Dr. Liu Chen
Plasma Physics Lab.
Princeton University
Princeton, New Jersey 08540

Dr. H. Okuda
Plasma Physics Lab.
Princeton University
Princeton, New Jersey 08540

Mrs. Elizabeth Graydon
Plasma Physics Library
Princeton University
Princeton, New Jersey 08540

Dr. Homer Meier
ORNL, P.O. Box 5
Bldg. 9201-2
Oak Ridge, Tenn. 37830

Dr. Robert Dory
ORNL, P.O. Box 5
Oak Ridge, Tenn. 37830

Ms. Cathy Mook
ORNL
Thermonuclear Library
Oak Ridge, Tenn. 37830

Dr. Erick Lindman
T-6, Los Alamos Sci. Lab.
Los Alamos, New Mexico 87544

Dr. Clair Nielson
Group CTR-6
Los Alamos Scientific Lab.
Los Alamos, New Mexico 87544

Ms. Betty W. Burnett
Main Library
Los Alamos Scientific Lab.
Los Alamos, New Mexico 87544

Dr. S. Gitomer
Plasma Research
Los Alamos Scientific Lab.
Los Alamos, New Mexico 87544

Dr. H.R. Lewis
Plasma Research
Los Alamos Scientific Lab.
Los Alamos, New Mexico 87544

Prof. Bernard Rosen
Stevens Institute
Hoboken, New Jersey 07030

Prof. Jacques Denavit
Mechanical Engr. Dept.
Northwestern University
Evanston, Illinois 60201

Dr. Jay Boris
Code 7750
U.S. Naval Research Lab.
Washington, D.C. 20375

Dr. Niels Winsor
Code 7750
U.S. Naval Research Lab.
Washington, D.C. 20375

Dr. Roswell Lee
Code 7750
U.S. Naval Research Lab.
Washington, D.C. 20375

Dr. Henry Klein
Science Applications Inc.
1200 Prospect St.
P.O. Box 2351
La Jolla, Ca. 92037

Dr. John McBride
Science Applications Inc.
1200 Prospect St.
P.O. Box 2351
La Jolla, Ca. 92037

Dr. Carl E. Wagner
Science Applications Inc.
1200 Prospect St.
P.O. Box 2351
La Jolla, Ca. 92037

Dr. Jeno Gazdag
I.B.M.
2670 Hanover St.
Palo Alto, Ca. 94320

Dr. Jose Canosa
Laboratorios ITT de Standard
Electrica, S.A.
Avda de America Km. 7,200
Madrid, Spain - 27

Dr. William Gough
EPRI, P.O. Box 10412
3412 Hillview Ave.
Palo Alto , Ca. 94304

Dr. Joanne Helton
Fusion Division
G.A., P.O. Box 608
San Diego, Ca. 92112

Library
c/o Tommey
General Atomic Company
P.O. Box 81606
San Diego, Ca. 92138

Prof. R.W. Hockney
Dept. of Computer Science
University of Reading,
Whiteknights, Reading RG6 2AX
ENGLAND

Dr. J.W. Eastwood
Dept of Computer Science
University of Reading,
Whiteknights, Reading RG6 2AX
ENGLAND

Dr. Dieter Biskamp
Max Planck Institute fur
Plasmaphysik
Garching bei Munchen, 8046
W. GERMANY

Dr. Keith V. Roberts
Culham Laboratory
Abingdon, Berks
ENGLAND

Dr. Dennis W. Hewett
Mail Stop 642
Los Alamos Scientific Lab
Los Alamos, N.M. 87545

Dr. Akira Hasegawa
Bell Telephone Labs
Murray Hill, New Jersey

Prof. Abraham Bers
Rm 20, B120
M.I.T.
Cambridge, Mass. 02139

Dr. George L. Johnston
M.I.T., Rm 38-256
Cambridge, Mass. 02139

Prof. Alan Macmahon
Physics Dept.
University of Texas, Austin
Austin, Texas 78710

Dr. W. Horton
Physics Dept.
University of Texas, Austin
Austin, Texas 78710

Prof. Georg Knorr
Physics and Astronomy Dept.
University of Iowa
Iowa City, Iowa 52242

Dr. W. Kruer
L545
LLL, U.C.B. Campus Mail

Dr. Claire Max
L545
LLL. U.C.B. Campus Mail

Dr. Harold Grad
New York University
Courant Inst. of Math Sciences
Magneto-Fluid Dynamic Div.
251 Mercer St.
New York, N.Y. 10012

Dr. S. Cuperman
Department of Physics and
Astronomy
Tel-Aviv University
Ramat-Aviv
Tel-Aviv, ISRAEL

W. E. Hobbs
Mission Research Corp.
P.O. Drawer 719
Santa Barbara, CA 93102

Dr. A. Sternlieb
Dept. of Physics & Astro.
University of Maryland
College Park MD 20740

Dr. John Guillory
Dept. of Physics & Astro.
University of Maryland
College Park MD 20740

Jae Koo Lee
EECS Dept. 119 MD Cory Hall
U.C.B. Campus Mail

Dr. William S. Cooper
LBL, Dept. 9454
Bldg. 16-110
U.C.B. Campus Mail

Dr. Gary Smith
L439
LLL, UCB
CAMPUS MAIL

Dr. Judith A. Harte
L545
LLL, U.C.B. Campus Mail

Dr. Bruce Cohen
L439
LLL, U.C.B. Campus Mail

Dr. John C. Taylor
L318
LLL, U.C.B. Campus Mail

Dr. Michael Gerver
c/o Prof. Ravi Sudan
Laboratory of Plasma Studies
Cornell University
Ithaca, N.Y. 14850

Dr. James R. Albritton
Laser Lab
University of Rochester
Rochester, N.Y. 14627

Dr. David Forslund
Mail Stop 642
Los Alamos Scientific Lab
Los Alamos, N.M. 87545

Dr. T. A. Lin
Physics Department
UCLA, Los Angeles, Ca. 90024

Dr. Nat Rynn
Dept of Physics
U.C. Irvine
Irvine, Ca.

Dr. Frank Hohl, Dir.
Space Physics Branch
Environmental & Space Sci. Div.
NASA - Langley Research Center
Hampton, Va. 23665

Dr. J. R. Freeman
Div. 5241
Sandia Laboratories
Albuquerque, New Mexico 87115

Dr. J. W. Poukey
Div. 5241
Sandia Laboratories
Albuquerque, New Mexico 87115

Oscar Manley
Fusion Plasma Theory Branch
Applied Plasma Physics Prgm.
Div. of Magnetic Fusion Energy
ERDA Headquarters
Germantown, Maryland 20767

R. N. Aiyer
Bhabha Atomic Research Centre
Laser Section
Modular Labs.
Trombay, Bombay 400 085
INDIA

Richard Briggs
L306
LLL, U.C.B. Campus Mail

Ed Lee
L306
LLL, U.C.B. Campus Mail

Frank Chambers
L306
LLL, U.C.B Campus Mail

Dr. Brendon Godfrey
Mail Stop 642
Los Alamos Scientific Lab
Los Alamos, N.M. 87545

Dr. C. E. Rathmann
Mission Research Corp
735 State Street
Post Office Drawer 719
Santa Barbara, Ca. 93102

Dr. Alex Friedman
Laboratory of Plasma Studies
c/o Prof. Ravi Sudan
Cornell University
Ithaca NY 14850

Capt. Erle Pettus
AFWL/DYP
Kirtland AFB, N.M. 87117

J. Leon Shohet
Dept. of Electrical
& Computer Engineering
The University of Wisconsin
Madison, Wisconsin 53706
Telephone: (608) 262-1191
(FTS) 262-1191 Direct

Dr. Carol Tull
L402, LLL
U.C.B. Campus Mail

Dr. Dwight Nicholson
Science Applications, Inc.
934 Pearl St., Suite A
Boulder, Colorado 80302

David Tetreault
MIT 36-229
Cambridge, Mass. 02139

Dr. William Tang
PRINCETON UNIVERSITY
Plasma Physics Laboratory
Princeton NJ 08540

Dr. Doren W. Padgett
Physics Program - *Code 421*
Office of Naval Research
Department of the Navy
Arlington VA 22217

Dr. F. R. Scott
EPRI, P.O. Box 10412
3412 Hillview Ave.
Palo Alto CA 94304

Dr. W. M. Fawley
Dept. of Astronomy
UNIVERSITY OF PENNSYLVANIA
Philadelphia PA 19104